Title: Retrograde mitochondrial transport is required for mitochondrial biogenesis in zebrafish neurons

Authors: Angelica E Lang[1, 2], Chris Stein[1], Roger Schultz[1, 3], and Catherine M Drerup[1, 2, 3, *]

Affiliations:

[1] Department of Integrative Biology; University of Wisconsin-Madison; Madison, WI 53706

[2] Genetics training program; University of Wisconsin-Madison; Madison, WI 53706

[3]Neuroscience training program; University of Wisconsin-Madison; Madison, WI 53706

*Corresponding author. Email: drerup@wisc.edu

Abstract: To maintain a functional mitochondrial population in a long-lived cell like a neuron, mitochondria must be continuously replenished through the process of mitochondrial biogenesis. Because most mitochondrial proteins are nuclear encoded, mitochondrial biogenesis requires communication between mitochondria and the nucleus. This can be a challenge in a large, compartmentalized cell like a neuron in which a large portion of the mitochondrial population is in neuronal compartments far from the nucleus. Using in vivo assessments of mitochondrial biogenesis in zebrafish neurons, we determined that mitochondrial transport between distal axonal compartments and the cell body is required for sustained mitochondrial biogenesis. Estrogen-related receptor transcriptional activation links transport with nuclear expression of mitochondrial genes. Together, our data support a role for retrograde feedback between axonal mitochondria and the nucleus for regulation of mitochondrial biogenesis in neurons.

Introduction

Mitochondria are critical for neuronal function and survival. These organelles have many essential roles, including production of ATP, calcium buffering, and the production of metabolites that can function as signaling molecules [1]. For a neuron to maintain a functional mitochondrial population, mitochondria must be replenished through the process of mitochondrial biogenesis [2]. In other cell types, such as myocytes and adipocytes, indicators of mitochondrial health and function like AMP/ATP and NAD+/NADH ratios as well as calcium signaling stimulate the transcriptional control of mitochondrial biogenesis in the nucleus [3-6]. These upstream signals can activate transcriptional regulators like the PGC-1 (Peroxisome Proliferator-activated Receptor Gamma Coactivator 1) family of transcriptional coactivators [7]. PGC-1α, considered the master regulator of mitochondrial biogenesis, can be activated by phosphorylation or de-acetylation by AMP-activated protein kinase (AMPK) or Sirtuin 1 (SIRT1) respectively [3,4,6]. AMPK activity is stimulated by increases in the AMP/ATP ratio while SIRT1 activity depends on local NAD+ levels. Once activated, PGC-1α can induce the expression of nuclear-encoded mitochondrial proteins through the activation of transcription factors like the nuclear respiratory factors (NRF1/2) or the estrogen related receptors (ERRα/β/γ) [7-10]. How neurons, with mitochondrial populations spread throughout dendritic and axonal arbors, oftentimes large distances from the nucleus, sense mitochondrial health and function to activate these transcriptional pathways is an open and critical question [2].

Mitochondrial biogenesis requires the division and expansion of existing organelles to increase mitochondrial mass. This requires the coordination of several cellular processes. Mitochondrial DNA (mtDNA) must be replicated and the mtDNA nucleoids segregated, after which mitochondrial fission occurs at or near the middle of the organelle [11,12]. Daughter mitochondria are expanded through transcription, translation, and mitochondrial import of nuclear encoded gene products as well as cellular and mitochondrial derived lipids [2,13]. Mitochondria also synthesize proteins encoded by mtDNA (thirteen in vertebrates) in the mitochondrial matrix. Given the dependence on coordinated mitochondrial and nuclear gene expression, it is unsurprising that a substantial amount of mitochondrial biogenesis occurs in the perinuclear region in non-neuronal cells [14,15]. In neurons, evidence of mitochondrial biogenesis, including mtDNA replication and synthesis of mitochondrial proteins, has been observed in both the neuronal cell body and in axons of chick, rat, and drosophila [13,16-19]. Local mitochondrial biogenesis is thought to support short-term, local changes in energy need at the synapse [16,19,20]. The respective contributions of cell body-based verses local mitochondrial biogenesis for support of synaptic mitochondrial populations is still a subject of investigation. For both, however, nuclear expression of mitochondrial genes would be required to produce the >1000 proteins necessary for functional organelles.

Mitochondria are actively transported between the cell body and axon terminal by microtubule-based transport. In neuronal axons, kinesin motor proteins are responsible for axon terminal directed (anterograde) mitochondrial transport while the Cytoplasmic dynein motor transports mitochondria from the periphery back to the cell body (retrograde) [21-24]. A complement of proteins including Trak1/2 and Miro1/2 have been shown to scaffold mitochondria to these motors for transport [25-31]. Disrupting mitochondrial transport into the axon impairs axon development and regeneration after injury [32-34]. Inhibition of retrograde mitochondrial transport from neurites back to the cell body causes mitochondrial accumulation in axonal and dendritic processes and impaired mitochondrial health at the synapse [35-37]. However, the role of retrograde

mitochondrial transport in mitochondrial population maintenance in neurons remained undefined.

We hypothesized that transport of mitochondria from distal regions of the neuron to the cell body could link mitochondrial population surveillance and regulation of mitochondrial biogenesis frequency in neurons. Using zebrafish neurons, we show that reducing mitochondrial retrograde transport from the axon terminal back to the cell body reduces markers of mitochondrial biogenesis, including mtDNA replication, nuclear transcription of mitochondrial genes, and the production of mitochondrial biomass in the cell body. mtDNA replication is also reduced in the axon terminal, suggesting both local and cell body-based mitochondrial biogenesis may be disrupted. Analysis of mitochondrial turnover at the synapse revealed that reduced mitochondrial biogenesis correlates with reductions in cell body-derived mitochondrial material transported to the axon terminal. Widespread disruption to mitochondrial gene expression in neurons lacking mitochondrial retrograde transport suggests transport plays an important role in regulation of transcriptional programs necessary for mitochondrial biogenesis. We present evidence that this crosstalk is mediated by NAD+/SIRT1-mediated deacetylation of Estrogen related receptors (ERR) which regulates ERR-dependent transcriptional activity. Together, our work supports a model in which the retrograde transport of mitochondria is a powerful signaling mechanism to regulate mitochondrial biogenesis in neurons.

Results

Inhibiting mitochondrial retrograde transport disrupts markers of mitochondrial biogenesis in neuronal cell bodies

We used larval zebrafish posterior lateral line (pLL) sensory neurons to study the dynamics of mitochondrial biogenesis in vivo. The pLL system is composed of afferent neurons and sensory organs called neuromasts situated along the trunk [38]. The cell bodies of pLL neurons are clustered in a ganglion (pLLg) near the head while the afferent axons extend down the body and branch into axon terminals that innervate neuromasts (Fig. 1a). Axon extension and synapse formation occurs by 4 days post fertilization (dpf; [39]), allowing us to use this system to study mitochondrial populations in a fully formed neuronal circuit in the translucent zebrafish larva. To disrupt retrograde mitochondrial transport in pLL neurons, we used an existing mutant line with a unique loss of function mutation in the gene encoding Actr10 (*actr10*^{nl15}; hereafter referred to as *actr10;* [35,37]). Actr10 is a component of the Cytoplasmic dynein accessory complex dynactin. Complete loss of Actr10 function results in failed cell division, likely due to loss of all dynein motor function [40]. In contrast, the *actr10*^{nl15} mutation in zebrafish causes loss of mitochondrial interaction with the dynein motor, leading to loss of retrograde (cell body directed) mitochondrial transport and accumulation of mitochondria in axon terminals ([35]; Fig. 1b, c). This disruption is specific to mitochondria, as other retrogradely moving cargos, including late endosomes, lysosomes, and signaling molecules, are transported normally. Additionally, transmission electron microscopy (TEM) analysis showed accumulations of only mitochondria in axon terminals [35]. Intriguingly, in addition to mitochondrial accumulation in the distal axons, we found a severe reduction in mitochondrial density (mitochondrial area/cytosolic area) in the cell body of *actr10* neurons (Fig. 1b, c). We asked if this loss of mitochondrial density could be due to loss of mitochondrial biogenesis in *actr10* mutants.

Mitochondrial biogenesis requires coordinated transcription of nuclear encoded mitochondrial genes. This is largely controlled by the PGC-1 family of transcriptional coactivators and their associated transcription factors, including NRF-1/2. Downstream of this transcriptional

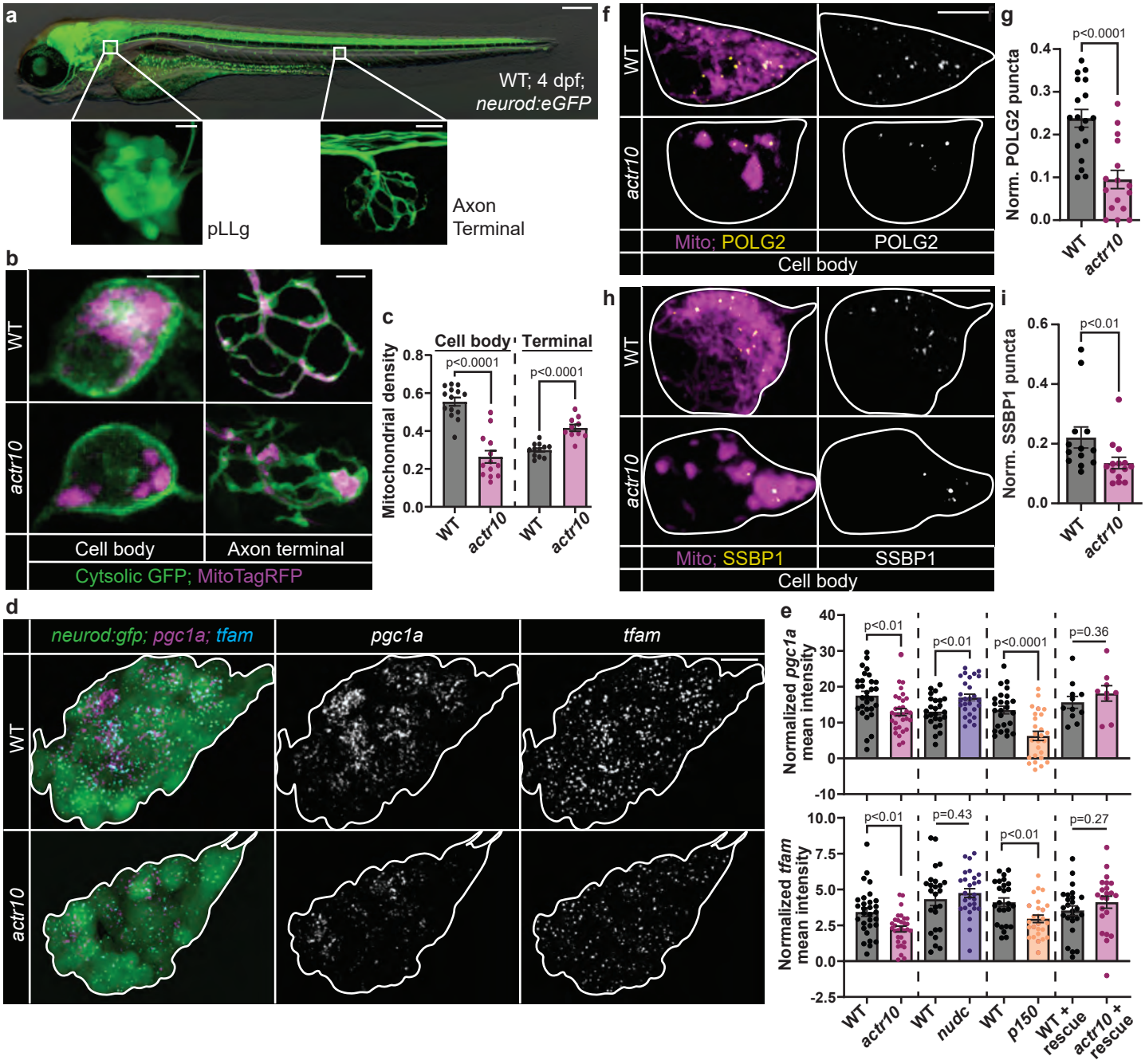

Figure 1: Mitochondrial cell body density and biogenesis markers are reduced in *actr10* mutants. (a) 4 dpf zebrafish transgenic larva carrying the *TgBAC(neurod:egfp)*^{nl1} transgene which labels neurons with GFP. The posterior lateral line gangion (pLLg) and a pLL axon terminal are boxed and magnified. (b) 4 dpf pLLg cell body and pLL axon terminal expressing cytosolic GFP and mitochondria-localized TagRFP (MitoTagRFP, magenta) in wild type and *actr10* mutants. (c) Quantification of mitochondrial density (mitochondrial area/cytosolic area; ANOVAs). (d) HCR RNA FISH labeling of *pgc1a* and *tfam* mRNA in the pLLg of wild type and *actr10* mutants carrying the *TgBAC(neurod:egfp)*^{nl1} transgene (white outline). (e) pLLg mean fluorescence intensity of *pgc1a* and *tfam* normalized to background (ANOVAs) in wild type, *actr10*, *nudc*, *p150*, and wild type/*actr10* larvae expressing Actr10 in neurons (+ rescue). (f) pLL cell body (outlined) expressing POLG2-GFP and mitoTagRFP (Mito, Magenta). (h) SSBP1 immunostaining in pLL cell body mitochondria, visualized with mitochondria-localized GFP (Mito, magenta; cell outlined). (g, i) Number of POLG2 or SSBP1 puncta normalized to mitochondrial volume (Wilcoxon). Scale bars: (a) full larva = 200 µm, insets = 10 µm; (b, f, & h) = 5 µm; (d) = 10 µm. All data are mean ± SEM and points represent individual larvae.

activation is a plethora of nuclear-encoded mitochondrial genes, including *tfam* [7,10]. We first assessed the expression of *pgc1a*, *pgc1b*, *nrf1*, and *tfam* using colorimetric in situ hybridization and found that all were noticeably reduced in *actr10* mutants (Supplementary Fig. 1a, b). To quantify gene expression of biogenesis markers in the pLLg, we turned to hybridization chain reaction RNA fluorescence in situ hybridization (HCR RNA FISH; [41]). We assessed *pgc1a* and *tfam* expression and confirmed both were significantly reduced in *actr10* mutants (Fig. 1d, e). Neuronal rescue of Actr10 in a stable transgenic line (*Tg(5kbneurod:mRFP-actr10)*^{nl22}; [35]) rescued neuronal mitochondrial density (Supplementary Fig. 1c, d) as well as *pgc1a* and *tfam* expression (Fig. 1e) confirming loss of Actr10 in neurons underlies this phenotype. To determine if the changes to gene expression in *actr10* mutants could be explained by general disruptions to retrograde cargo transport, we quantified gene expression in control mutant strains with loss of function mutations in *p150a/b* (duplicated gene in teleost fish requiring double knockout) and *nudc* [35,42]. p150 is a component of the dynactin complex that, when mutated, disrupts all retrograde cargo transport, including mitochondria [35,43-45]. NudC is a dynein regulator that, when mutated in zebrafish neurons, disrupts the retrograde transport of late endosomes and autophagosomes without altering the localization or transport of mitochondria [42]. *pgc1a* and *tfam* expression were reduced in *p150* mutants but unaffected in *nudc* mutants, further suggesting the decreased expression of these mitochondrial biogenesis markers was due to the loss of retrograde mitochondrial transport (Fig. 1e).

We next analyzed a critical step during biogenesis, mtDNA replication, using POLG2-GFP, a fluorescently tagged version of the processivity subunit of the mitochondrial DNA polymerase. POLG2-GFP has been previously shown to specifically localize to mtDNA nucleoids actively undergoing replication [12,46]. We expressed POLG2-GFP in pLL neurons and quantified the number of puncta, indicative of replicating mtDNA nucleoids, relative to mitochondrial volume. The number of POLG2 puncta was significantly reduced in *actr10* pLL cell body mitochondria, indicative of reduced mtDNA replication (Fig. 1f, g). To confirm these results, we performed immunolabeling for single stranded binding protein 1 (SSBP1), which transiently associates with mtDNA to facilitate replication [47]. The number of SSBP1 puncta relative to mitochondrial volume was significantly reduced in *actr10* pLL cell bodies (Fig. 1h, i). This phenotype is not due to loss of mtDNA as the density of nucleoids labelled with the mtDNA nucleoid protein TFAM (transcription factor A, mitochondria; [48]) is not decreased in *actr10* cell body mitochondria (Supplementary Fig.1e, f). As expected, due to the reduced mitochondrial density in the cell body and in line with loss of *tfam* mRNA based on HCR RNA FISH quantification, overall number of TFAM puncta are reduced in *actr10* mutant cell bodies (Supplementary Fig. 1g). mtDNA nucleoid size was unchanged between wild type and *actr10* mutants (Supplementary Fig. 1h). Together with our previous results demonstrating no deficits in measures of mitochondrial health and function in *actr10* mutant pLL neuronal cell bodies[37], this suggests decreases in mtDNA replication are not due to mitochondrial stress in the cell body. Mitochondrial biogenesis has also been demonstrated to occur in the distal axon through assessment of mtDNA replication [16,19,20]. To determine if local mitochondrial biogenesis was also affected in *actr10* mutants, we quantified mtDNA replication in the pLL axon terminal. Both POLG2 and SSBP1 puncta were significantly reduced in *actr10* mutants, suggesting both cell body and axon terminal mitochondrial biogenesis are disrupted by loss of retrograde mitochondrial transport (Supplementary Fig. 1i-l).

Nuclear transcription of mitochondrial genes is disrupted in actr10 mutant neurons

159 Given the changes to mtDNA replication and transcription of mitochondrial biogenesis related
160 genes, we decided to look more broadly at how nuclear gene expression of mitochondrial
161 proteins may be altered in *actr10* mutants. We isolated pLL neurons using fluorescence activated
162 cell sorting (FACS) from a novel transgenic line (*Tg(hsp70:eGFP-SILL)*^{uwd12Tg}; Supplementary
163 Fig. 2a, b) which expresses GFP in pLL neurons. FACS gating parameters were optimized to sort
164 true GFP-expressing cells and exclude autofluorescence particularly apparent in the yolk
165 (Supplementary Fig. c). We then performed bulk RNA-sequencing on FACS sorted cells to
166 analyze the transcriptomes of wild type and *actr10* mutant neurons (Fig. 2a). Differential gene
167 expression analysis and cross comparisons to the MitoCarta database confirmed that
168 mitochondrial genes are significantly downregulated in *actr10* mutants compared to wild type
169 siblings (Fig. 2b, c; [49]). In contrast, there were only 3 mitochondrial genes significantly
170 upregulated (p=0.999, Fisher's exact test). Gene Set Enrichment Analysis (GSEA) of Gene
171 Ontology terms identified Mitochondrial Protein Complexes to be the most significantly de-
172 enriched term in the dataset (Fig. 2d and Supplementary Fig. 2d) and KEGG pathway enrichment
173 analysis showed strong enrichment for mitochondrial pathways in downregulated genes
174 (Supplementary Fig. 2e). To confirm our RNA-seq results, we used HCR RNA FISH to quantify
175 pLL ganglion expression of ten downregulated genes and two genes that were not altered in our
176 dataset. These analyses aligned with our RNA-seq data, confirming loss of these mitochondrial
177 transcripts in *actr10* mutants (Fig. 2e-h). Additionally, we confirmed these results using
178 colorimetric in situ hybridization of a subset of these genes, showing reduced expression of
179 *atp5md* and *cox5ab* but not the controls *polb* and *tomm40* (Supplementary Fig. 2f, g). Finally, to
180 assess the specificity of the transcriptomic changes, we included positive and negative control
181 mutant strains *p150* and *nudc* described above [35,42]. As predicted, *p150* but not *nudc* mutants
182 have a loss of *cox5ab* expression (Fig. 2e, f). Together, this transcriptomic analysis suggests that
183 mitochondrial retrograde transport modulates nuclear expression of a subset of mitochondrial
184 genes.

185 *Impaired mitochondrial biogenesis decreases the contribution of cell body-derived mitochondria*
186 *to the axon terminal*

187 We next wanted to determine if these changes in measures of mitochondrial biogenesis translated
188 into a decrease in the production of new organelles. In neurons, we predicted that at least a
189 subset of mitochondria produced by biogenesis in the cell body would be transported in the
190 anterograde direction to support the population of mitochondria in the axon terminal [2]. To test
191 this, we used photo-labeling strategies to assess the rate of cell body-derived mitochondrial
192 addition to the axon terminal in wild type animals. We expressed photoactivatable GFP (PA-
193 GFP) localized to the mitochondrial matrix in pLL neurons and locally activated the GFP only in
194 the cell body. Then, we quantified the addition of cell body derived mitochondrial material to the
195 axon terminal at multiple time-points after photo-activation. We found that by 4 to 8 hours post-
196 activation (hpa), ~50% of the mitochondrial density in the axon terminal contained material that
197 was cell body-derived (Supplementary Fig. 3a-d). Next, we asked if the amount of cell body-
198 derived mitochondrial material transported to the axon terminal correlated with turnover of the
199 axon terminal mitochondrial population. Published data has shown that axon terminal
200 mitochondria are consistently lost over a period of hours in pLL axon terminals [37]. Using precise
201 activation of matrix-localized PA-GFP in axon terminal mitochondria followed by post-
202 activation imaging, we determined that ~50% of the labeled mitochondrial density is absent from
203 the axon terminal by 8 hpa (Supplementary Fig. 3e-g). This complements the estimated rate of
204 mitochondrial entrance into the axon terminal from the cell body and suggests that cell body-

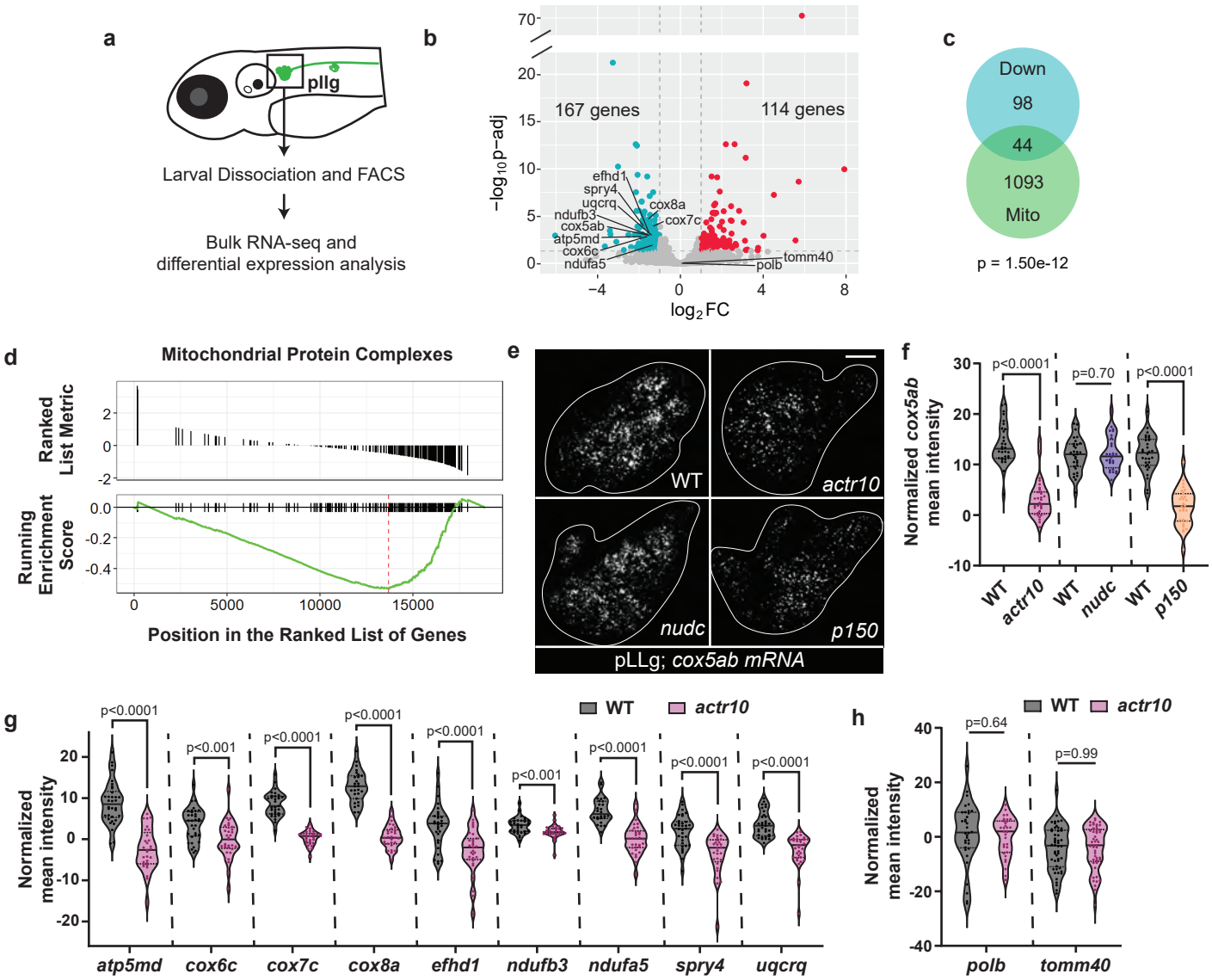

Figure 2: Mitochondrial gene expression is downregulated in *actr10* mutants. (a) RNA-sequencing strategy. (b) Volcano plot showing differential gene expression between wild type and *actr10* mutants. The plot shows -log10(adjusted p-value) vs. log2(Fold Change). Blue dots represent genes significantly downregulated while red dots represent genes significantly upregulated in *actr10* mutants. Genes selected for secondary analysis using HCR RNA FISH are labeled. (c) Overlap between downregulated genes and the MitoCarta3.0 database of the mitochondrial proteome (Fisher's exact test). Human homologs of downregulated zebrafish genes were used for analysis. Duplicated zebrafish paralogues were only counted once. (d) GSEA plot for Mitochondrial Protein Complexes, the most significantly de-enriched gene ontology term in *actr10* mutants relative to wild type. (e) Representative images of HCR RNA FISH labeling of *cox5ab* mRNA in the pLLg (outlined in white) for wild type, *actr10*, *nudc*, and *p150* mutants. Scale bar = 10 µm. (f) pLLg mean fluorescence intensity of *cox5ab* normalized to background (ANOVAs). (g) pLLg mean fluorescence intensity normalized to background for downregulated mitochondrial genes in wild type vs. *actr10* mutants (ANOVAs). (h) pLLg mean fluorescence intensity normalized to background for control genes in wild type vs. *actr10* mutants (ANOVAs). (f-h) Data plot lines represent the median and quartiles; data points represent individual larvae.

derived mitochondria may play a significant role in maintenance of the axon terminal mitochondrial population.

Given the role for cell body-derived mitochondria in axon terminal turnover, we predicted that decreased biogenesis in the cell body would result in a progressive loss of mitochondrial addition to the axon terminal. To test this, we assessed changes to mitochondrial biogenesis and transport in *actr10* mutants across multiple timepoints post-axon extension (2, 3, and 4 dpf). Initial axon extension of primary pLL axons is complete by 2 dpf with functional synapses apparent by 4 dpf [38,39,50]. Assessment of mitochondrial density in axon terminals and cell bodies of *actr10* mutants demonstrated that mitochondrial density was elevated in axon terminals as early as 2 dpf (Supplementary Fig. 4a, b) and cell body mitochondrial density was notably depleted by 3 dpf (Supplementary Fig. 4c, d). Quantification of the biogenesis markers *pgc1a* and *tfam* using HCR RNA FISH demonstrated that loss of cell body mitochondrial density at 3 dpf corresponded with loss of *pgc1a* expression, followed by loss of *tfam* expression by 4 dpf (Fig. 1d, e and Supplementary Fig. 4e, f). This time course confirms that loss of cell body mitochondrial density correlates with decreased markers of mitochondrial biogenesis.

We predicted that the progressive loss of cell body mitochondrial biogenesis in *actr10* mutants would result in reduced anterograde mitochondrial transport. Live imaging of mitochondrial movement in pLL axons demonstrated that retrograde transport was disrupted at 3 dpf while anterograde transport frequency was not altered until 4 dpf (Supplementary Fig. 4g, h and Supplementary Movies 1-4). This time series demonstrated retrograde mitochondrial transport is lost first in *actr10* mutants, leading to mitochondrial accumulation in the axon terminal. Only after retrograde mitochondrial transport is inhibited does mitochondrial biogenesis fail, leading to loss of cell body mitochondria and reduced anterograde transport of mitochondria towards axon terminals (summarized in Supplementary Fig. 4i).

Together, our data suggest that anterograde mitochondrial transport supplies the axon terminal with cell body-derived mitochondria produced through biogenesis. To test this, we directly stimulated mitochondrial biogenesis and analyzed axon terminal mitochondrial addition. To increase mitochondrial biogenesis, we used a stable transgenic zebrafish line overexpressing human PGC-1α in neurons (*Tg(-5kbneurod1:PGC1α-2A-mRFP)*^{uwd9Tg}; [51]). PGC-1α overexpression in this line increased *tfam* expression in pLL neurons and has been previously shown to increase mitochondrial density in the axon terminal, confirming increased mitochondrial biogenesis (Supplementary Fig. 4j; [51]). To determine if increased mitochondrial biogenesis increases the addition of cell body-derived mitochondria to the axon terminal, we used photoconversion and mitochondrial tracking. For this, we used a dual transgenic line expressing PGC-1α (*Tg(-5kbneurod1:PGC1α-2A-mRFP)*^{uwd9Tg}) and mEos, a photoconvertible protein, localized to the mitochondrial matrix (*Tg(-5kbneurod1:mito-mEos)*^{y586Tg}; [37,52]). We photoconverted the mitochondrial population in the pLL ganglion at 4 dpf and imaged axon terminals 4 hours post-conversion (hpc; Fig. 3a). By 4 hpc, cell body-derived mitochondrial density in the axon terminal was significantly increased in PGC-1α transgenics, confirming that mitochondrial biogenesis in the cell body impacts mitochondrial addition to the axon terminal population (Fig. 3b, c). Next, we assessed the density of cell body-derived mitochondria in *actr10* mutant axon terminals using the same photoconversion strategy. This demonstrated a 50% reduction in the contribution of cell body-derived mitochondria to the axon terminal population in *actr10* mutants compared to wild type (Fig. 3b, c).

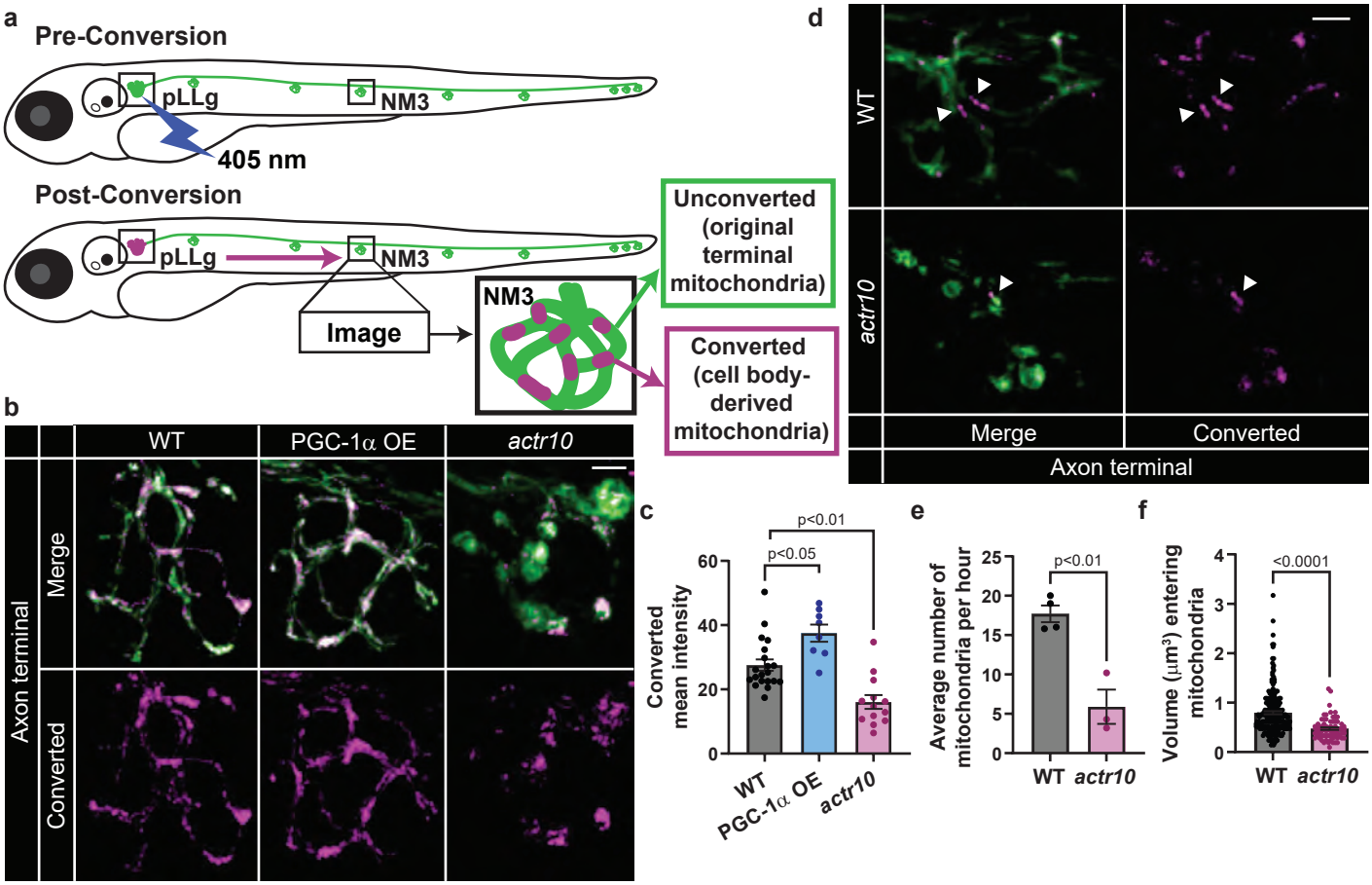

Figure 3: Cell body-derived mitochondrial density in the axon terminal is reduced in *actr10* mutants. (a) Photoconversion strategy. Mitochondrial matrix-localize mEos in the pLLg was locally converted using 405 nm laser. An axon terminal in the mid-trunk (neuromast 3 - NM3) was imaged 4 hpc (b) or every minute for 6h (d). (b) NM3 4 hpc in wild type, *actr10*, and transgenic overexpressing (OE) PGC-1α in neurons *(Tg(-5kbneurod1:PGC1α-2A-mRFP)^{uwd9})*. (c) Mean fluorescence intensity of cell body-derived mitochondria (Converted) in the axon terminal population (Steel-Dwass). (d) Representative timepoint of a pLL axon terminal from 6 hr timelapse video (Movies S5 and S6). Cell body-derived mitochondria indicated with white arrowheads. (e, f) Quantification of the number (e, ANOVA) and size (f, Wilcoxon) of converted mitochondria entering the axon terminal. Scale bars = 5 μm. All data are mean ± SEM. Data points represent individual larvae in c and e and individual mitochondria measured from 4 wild type and 3 *actr10* axon terminals in f.

249 Reduced cell body derived mitochondrial material in the axon terminal could be due to either
250 fewer mitochondria or smaller mitochondria being transported to the terminal. To differentiate
251 this, we tracked mitochondrial addition to the axon terminal using time-lapse imaging.
252 Mitochondria in the pLL ganglion carrying matrix localized mEos were photoconverted and the
253 axon terminal was imaged every minute for 6 hours (Supplementary Movies 5 and 6). *actr10*
254 mutants had both fewer and smaller cell body derived mitochondria entering the terminal per
255 hour (Fig. 3d-f). Together, this suggests mitochondrial biogenesis in the cell body contributes to
256 both number and size of new mitochondria transported to the axon terminal.
257
258 *Disrupted mitochondrial fission does not alter mitochondrial biogenesis signatures*
259 At the light microscopy level, mitochondria in *actr10* mutant pLL cell bodies appear to have a
260 more circular and aggregated morphology, which can be indicative of impaired fission (see Fig.
261 1b; [53,54]). To better understand the structure of pLL neuron cell body mitochondria, we used
262 TEM to assess their ultrastructure in *actr10* mutants. In wildtype pLL cell bodies, mitochondria
263 were evenly distributed throughout the cytosol (Supplementary Fig. 5a). In *actr10* mutants, cell
264 body mitochondrial density and morphology were variable: some cell bodies had fewer but
265 significantly enlarged mitochondria (Supplementary Fig. 5b; 5/12 cell bodies), some showed a
266 more even distribution similar to wildtype (Supplementary Fig. 5c; 1/12 cell bodies), and some
267 showed no visible mitochondria (Supplementary Fig. 5d; 6/12 cell bodies). In contrast, even
268 wildtype cell bodies with little visible cytosolic area still had mitochondria present
269 (Supplementary Fig. 5e; 0/10 cell bodies with no visible mitochondria). On average,
270 mitochondria were significantly larger with a reduced number in *actr10* cell bodies
271 (Supplementary Fig. 5f, g). Altered mitochondrial structure could suggest impaired
272 mitochondrial health. However, previous work has shown *actr10* mutants have normal
273 mitochondrial health measures in the cell body, and our TEM images show normal cristae even
274 in the enlarged mitochondria (Supplementary Fig. 5b; [37]). Together, these data show that *actr10*
275 mutant mitochondria are larger and rounder than those in wild type siblings, despite not showing
276 altered measures of health and productivity [37].
277 Altered mitochondrial fission can result in large, circular organelles [53,54]. Given the relationship
278 between mitochondrial fission and mitochondrial biogenesis, we asked if disrupted
279 mitochondrial fission in *actr10* mutants could underlie disrupted mitochondrial biogenesis [11,12].
280 First, we assessed length of moving and stationary mitochondria in pLL axons in *actr10* mutants
281 and wild type siblings as a proxy for fission dynamics. These data showed no change in
282 mitochondrial length, suggesting no major changes in fission or fusion dynamics in the axon
283 (Supplementary Fig. 5h). The cell body mitochondria are too dense for us to directly measure
284 their length or assess fission frequency. Instead, we disrupted mitochondrial fission and assessed
285 measures of mitochondrial biogenesis. To disrupt mitochondrial fission, we expressed a
286 dominant negative form of Drp1 which mimics a constitutively GDP-bound form of the enzyme
287 ($Drp1^{K38A}$; [54,55]). In cultured cells, expression of $Drp1^{K38A}$ disrupts mitochondrial fission [54,55].
288 When expressed in pLL neurons, $Drp1^{K38A}$ causes clustering of mitochondria to the perinuclear
289 region of the cell body and reduces mitochondrial density in both wild type and *actr10* cell
290 bodies (Fig. 4a, b). However, $Drp1^{K38A}$ expression does not change measures of mitochondrial
291 biogenesis including *tfam* expression or the number of SSBP1 labeled replicating mtDNA
292 nucleoids (Fig. 4c-f). These data argue that loss of fission is not causal in the *actr10* mutant
293 mitochondrial biogenesis phenotype.
294 *MitoTruck mediated disruption of mitochondrial transport inhibits mitochondrial biogenesis*

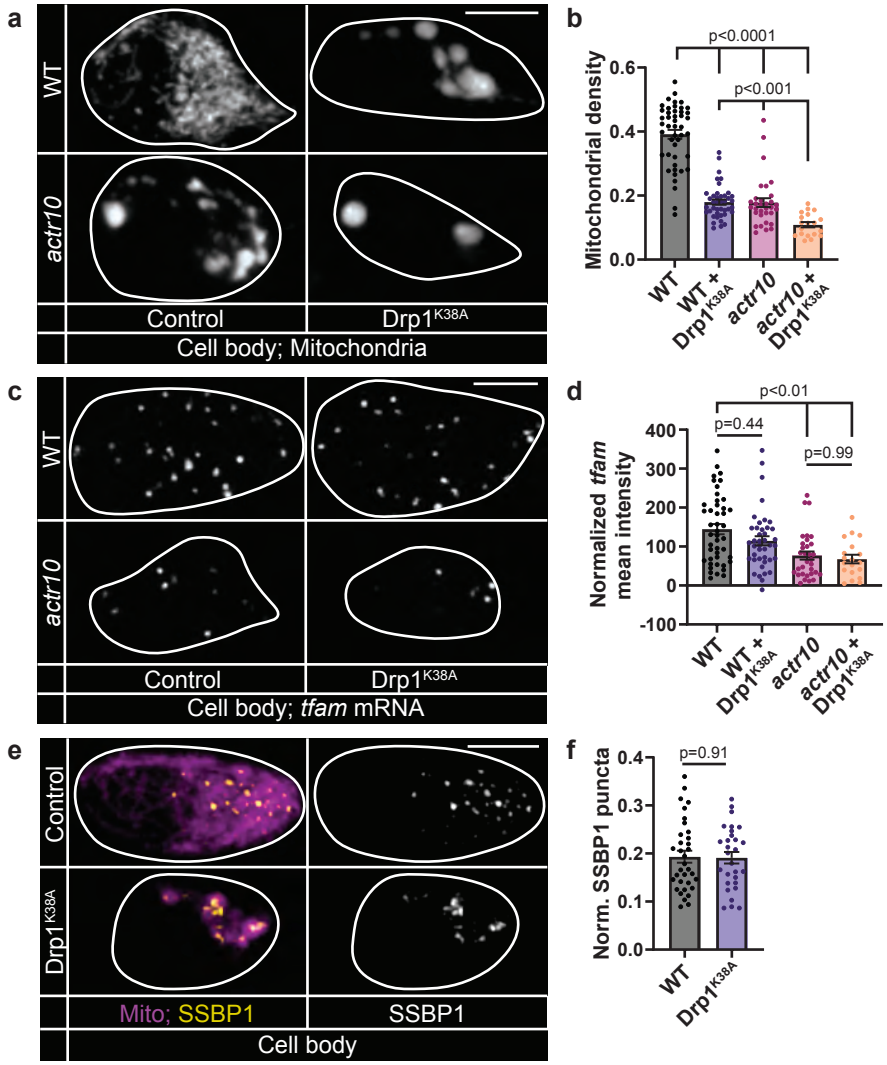

Figure 4: Disrupting mitochondrial fission does not alter *tfam* expression or mtDNA replication. (a) Single pLL cell bodies (outlined) expressing mitoTagRFP in wild type and *actr10* mutant larvae expressing Drp1^{K38A}-RFP or RFP (control). (b) Quantification of mitochondrial density (mitochondrial area/cytosolic area; Steel-Dwass). (c) HCR RNA FISH labeling of *tfam* mRNA in a pLL cell body (outlined). (d) Mean fluorescence intensity of *tfam* normalized to background (Steel-Dwass). (e) SSBP1 immunostaining in pLL cell body mitochondria, visualized with mitochondria-localized GFP (Mito, magenta; cell outlined). (f) Number of SSBP1 puncta normalized to mitochondrial volume (ANOVA). All data are mean ± SEM. Data points represent individual larvae.

295 Our data demonstrate that inhibiting mitochondrial return to the cell body impairs mitochondrial
296 biogenesis. To test this in another model, we engineered a synthetic tether, similar to one
297 previously described in *C. elegans,* to constitutively move mitochondria out of the cell body and
298 inhibit their ability to return to the cell body from the distal axon (MitoTruck; [56]). For this, we
299 tethered mitochondria to a constitutively active kinesin motor domain derived from KIF1A using
300 the OMP25 outer mitochondrial membrane localization sequence (Fig. 5a; [57,58]). When expressed
301 in pLL neurons, MitoTruck localizes to mitochondria and ectopically concentrates these
302 organelles to axon ends, demonstrating anterograde transport bias (Fig. 5b). Constitutive
303 expression of MitoTruck caused failed axon extension and neuronal death by 4 dpf. To avoid any
304 phenotypes due to failed neuronal health, we analyzed mitochondrial parameters after 24 hours
305 of MitoTruck expression, at 2 dpf. Mitochondria in the cell body are significantly depleted in
306 MitoTruck expressing neuron cell bodies by 2 dpf (Fig. 5c, d). This depletion is similar to that
307 observed in *actr10* mutants at 4 dpf (mitochondrial density: WT 2 dpf 0.57 ± 0.018, MitoTruck 2
308 dpf 0.33 ± 0.016, WT 4 dpf 0.55 ± 0.027, *actr10* 4 dpf 0.26 ± 0.028). Analyses of mtDNA
309 replication and *tfam* expression demonstrated that MitoTruck significantly decreased these
310 markers of mitochondrial biogenesis (Fig. 5e-h). Together our *actr10* mutant and MitoTruck
311 analyses demonstrate that inhibiting mitochondrial return to the cell body from the axon is
312 sufficient to impair markers of mitochondrial biogenesis.

313 *Estrogen-related receptors bridge mitochondrial transport with transcriptional regulation of*
314 *mitochondrial biogenesis*

315 Our data indicate retrograde transport is required to promote mitochondrial biogenesis through
316 regulation of upstream factors including nuclear gene expression. Several nuclear transcription
317 factors have been identified that bind the promoters of a wide range of mitochondrial genes,
318 allowing for coordinated expression of these genes during biogenesis [10,59,60]. We hypothesized
319 that a key transcription factor could link mitochondrial retrograde transport to mitochondrial
320 biogenesis. To identify this transcription factor, we performed transcription factor enrichment
321 analysis using significantly downregulated genes from our RNA-seq dataset. This in silico
322 analysis identified Estrogen related receptors (ERRs) as top candidates (Fig. 6a and
323 Supplementary Fig. 6a). ERRs have been shown to be coactivated by PGC-1α to regulate
324 mitochondrial biogenesis [59,61-63]. Other transcription factors regulated by PGC-1α such as
325 NRF1/2 or PPARα were not found to be enriched in our analysis, suggesting ERRs specifically
326 may be affected in *actr10* mutants. To validate this result, we used gene set enrichment analysis
327 of transcription factor binding targets and identified the ERR binding motif ERR1 enriched near
328 downregulated genes (Supplementary Fig. 6b). Finally, we took a more targeted approach by
329 comparing our list of downregulated genes to ESRRG targets identified by ChIP-seq in cultured
330 neurons [63]. We found significant enrichment for known neuronal ESRRG target genes in our data
331 set (Fig. 6b). In contrast, there was only one target gene from the Chip-seq dataset that was
332 significantly upregulated in our dataset (p=0.885, Fisher's exact test). Together, these in silico
333 analyses suggest ERR-dependent transcription is reduced in *actr10* mutants.

334 If disruption of ERR-dependent transcription underlies decreased mitochondrial biogenesis in
335 *actr10* mutant neurons, increasing ERR activity should rescue this defect. To test this, we
336 overexpressed Esrra in pLL neurons and assessed mitochondrial density and biogenesis
337 transcriptional programs. Similar to PGC-1α overexpression (see Supplementary Fig. 4j; [51]),
338 Esrra overexpression significantly increased *tfam* expression (Supplementary Fig. 6c, e).
339 Furthermore, Esrra overexpression in *actr10* mutants rescues *tfam* expression to wild type levels

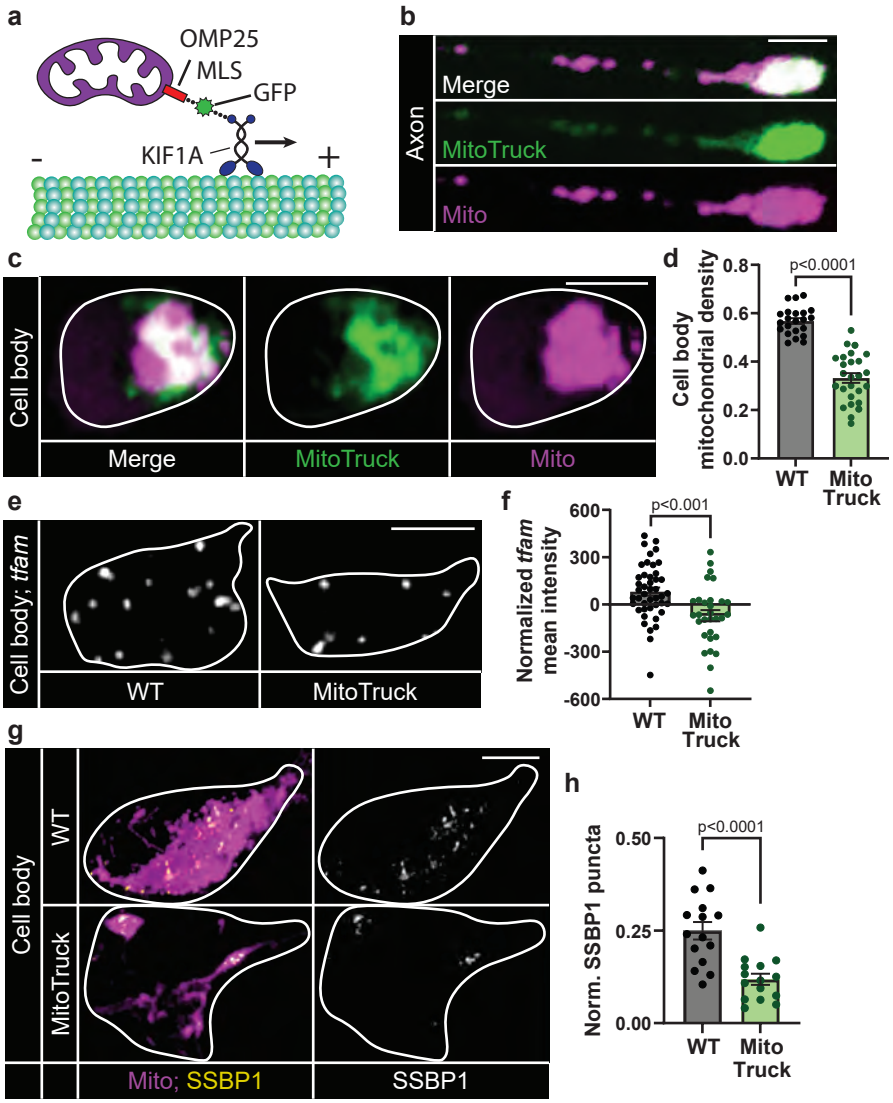

Figure 5: MitoTruck expression decreases cell body mitochondrial density and markers of mitochondrial biogenesis. (a) Schematic of the MitoTruck construct. The constitutively active KIF1A motor domain was tethered to mitochondria with the OMP25 outer mitochondrial membrane localization signal (MLS) and visualized with GFP. (b,c) pLL axon (b) and cell body (c; outlined) expressing MitoTruck (green) and MitoTagRFP (Mito, magenta). (d) Quantification of pLL cell body mitochondrial density (mitochondrial area/cytosolic area; Wilcoxon). (e) Representative images of HCR RNA FISH labeling of *tfam* mRNA in a single pLL cell body (outlined) without and with MitoTruck expression. (f) Mean fluorescence intensity of *tfam* normalized to background (ANOVA). (g) SSBP1 immunostaining in a single pLL cell body (outlined). Mitochondria visualized with mitochondrially localized TagRFP (Mito, magenta). (h) Number of SSBP1 puncta normalized to mitochondrial volume (ANOVA). Scale bars = 5 µm. All data are mean ± SEM and points represent individual larvae.

340 (Supplementary Fig. 6d, f). However, overexpression of Esrra was unable to rescue the loss of
341 cell body mitochondrial density in *actr10* mutants, suggesting additional levels of ERR
342 regulation are required for optimal mitochondrial biogenesis activation (Fig. 6c, d). Activation of
343 ERR-dependent transcription is modulated by ERR or PGC-1α posttranslational modifications
344 (PTMs). We hypothesized PTMs are required for full Esrra activity. The most well studied
345 modifications that activate this pathway are SIRT1-dependent deacetylation of ERR and/or PGC-
346 1α and AMPK-dependent phosphorylation of PGC-1α [64-68]. To determine if SIRT1 or AMPK
347 activation were upstream of ERR-dependent mitochondrial biogenesis in neurons, we treated
348 wild type and *actr10* mutant zebrafish with resveratrol (activator of SIRT1) or AICAR (activator
349 of AMPK) at concentrations previously optimized for use in zebrafish larvae [64,69,70]. Resveratrol,
350 but not AICAR, treatment was sufficient to rescue cell body mitochondrial load in *actr10* mutant
351 neurons (Fig. 6e, f and Supplementary Fig. 6g, h), suggesting SIRT1-mediated deacetylation of
352 ERRs may be disrupted in *actr10* mutants.

353 SIRT1 has been shown to deacetylate human ESRRA at 4 conserved lysine residues (amino
354 acids 129, 138, 160, and 162) within the DNA-binding domain. This deacetylation can be
355 mimicked by mutating the 4 lysine residues to arginine (4KR), which conserves the basic charge
356 of lysine but prevents acetylation[67]. Overexpression of Esrra^{4KR} in pLL neurons was able to
357 rescue *actr10* cell body mitochondrial density (Fig. 6c, d), similar to rescue by resveratrol,
358 suggesting deacetylation is critical for upregulation of mitochondrial biogenesis by Esrra. This
359 was further supported by the localization of Esrra protein. Wild type Esrra did not display a
360 canonical nuclear localization[71] and instead remained largely cytosolic. In contrast, Esrra^{4KR}
361 displayed strong nuclear localization, suggesting deacetylation is critical for nuclear localization
362 to subsequently activate mitochondrial biogenesis pathways (Fig. 6g, h). Further supporting a
363 role for deacetylation in Esrra-dependent mitochondrial biogenesis, overexpression of Esrra^{4KR}
364 fully rescues SSBP1 punctal density in *actr10* mutants (Fig. 6i, j). These data demonstrate that
365 ERR deacetylation is critical for regulation of mitochondrial biogenesis in pLL neurons.

366 SIRT1 is a nuclear-localized protein that is activated by elevated NAD+ levels[72]. To determine if
367 NAD+ levels were altered in *actr10* nuclei, we used a genetically encoded NAD+ sensor
368 localized to the nucleus[73]. Analysis of steady state NAD+ levels revealed a significant reduction
369 in nuclear NAD+ in *actr10* mutants (Fig. 7a, b). A significant pool of cellular NAD+ is stored in
370 mitochondria and changes to NAD+/NADH levels in mitochondria can affect the
371 cytosolic/nuclear pool [74-76]. We reasoned that altered mitochondrial transport could change local
372 mitochondrial NAD+ levels, leading to a reduction in local SIRT1 activation in the cell body. To
373 test this, we assessed mitochondrial NAD+ in the cell body and axon terminal of pLL neurons by
374 localizing the genetically encoded biosensor to the mitochondria matrix. We found significantly
375 elevated NAD+ levels in axon terminal mitochondria in *actr10* mutants while cell body
376 mitochondria have a significant reduction in mitochondrial NAD+ levels compared to wild type
377 controls (Fig. 7c-e). Finally, we asked if retrograde transport was responsible for moving
378 mitochondria with higher NAD+ measures from the axon terminal to the cell body. Using live
379 imaging, we assessed mitochondrial NAD+ levels in moving and stationary organelles using the
380 same NAD+ sensor. These experiments demonstrated that retrogradely moving mitochondria
381 have significantly higher NAD+ levels than either stationary or anterogradely moving
382 mitochondria (Fig. 7f, g). Together, our data support a model in which the mitochondria with
383 high levels of NAD+ returning to the cell body from the axon elevate local NAD+ levels to
384 activate SIRT1-dependent ERR transcriptional activity necessary for sustained mitochondrial
385 biogenesis in neurons (Fig. 7h). We propose that disrupting retrograde mitochondrial transport

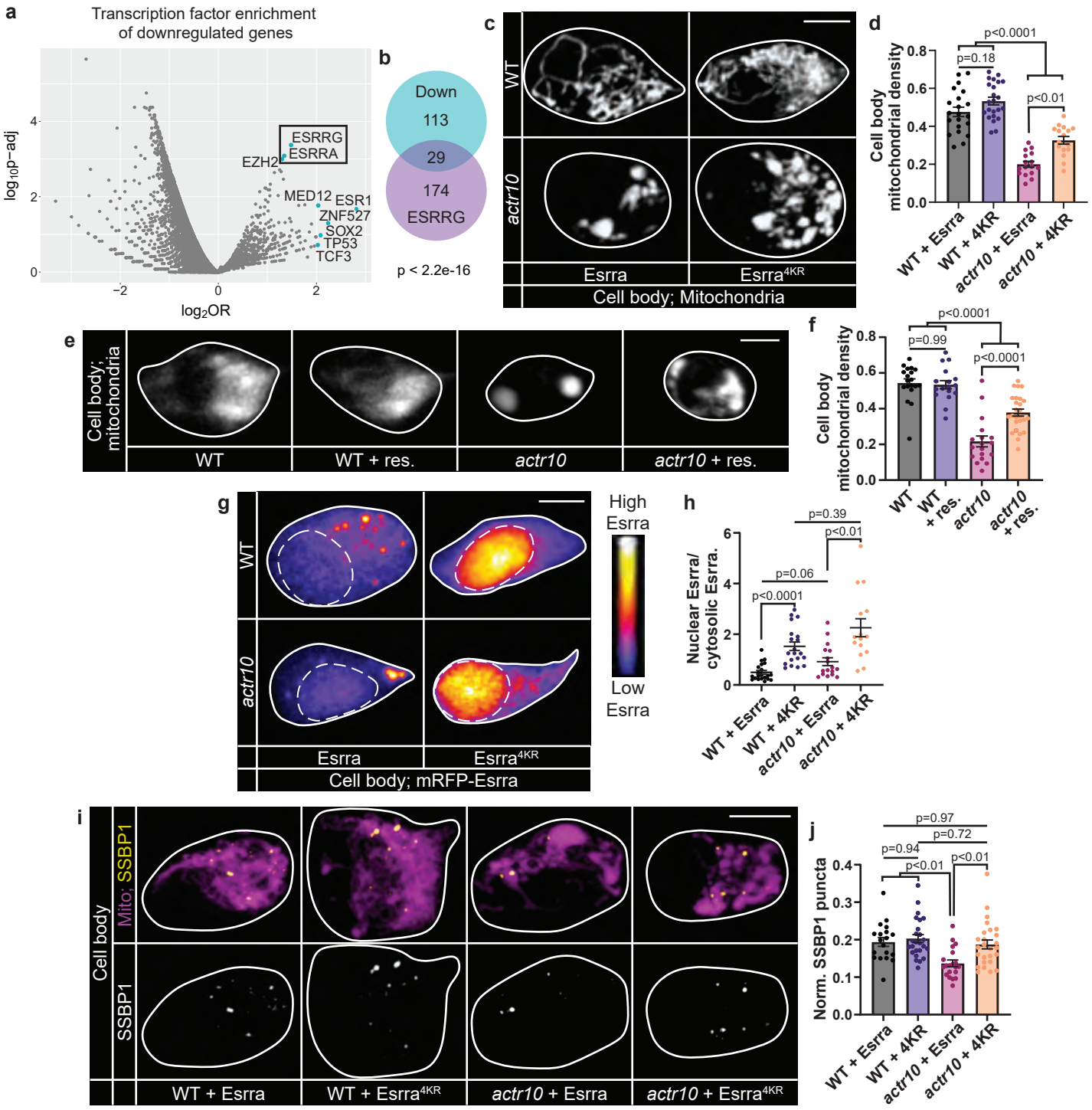

Figure 6: ERR activity links mitochondrial transport and mitochondrial biogenesis. (a) Transcription factor enrichment analysis for genes significantly downregulated in *actr10* mutants. Plot shows log2(Odds Ratio) vs. log10(adjusted p-value). Top 10 enriched genes based on euclidean distance from log2(OR)/log10(adj. p-value) to the origin are labeled. Box indicates ERR transcription factors identified in the dataset. (b) Overlap between downregulated genes and ESRRG neuronal ChIP-seq targets (Fisher's exact test). Human homologs of downregulated zebrafish genes were used for transcription factor analyses. Duplicated zebrafish paralogues were only counted once in the analysis. (c) Mitochondria in wild type and *actr10* pLL cell bodies (outlined) expressing Esrra or Esrra^{4KR}. (d) Quantification of mitochondrial density (ANOVAs; Tukey HSD). (e) Mitochondria in wild type and *actr10* pLL cell bodies (outlined) with and without resveratrol (+ res.) treatment. (f) Quantification of mitochondrial density (ANOVAs; Tukey HSD). (g) Heat map of mRFP-Esrra or mRFP-Esrra^{4KR} in wild type and *actr10* pLL cell bodies (outlined). (h) Mean fluorescence intensity of nuclear mRFP-Esrra/cytosolic mRFP-Esrra (Steel-Dwass). (i) SSBP1 immunostaining in pLL cell body mitochondria, visualized with mitochondria-localized GFP (Mito, magenta; cell outlined). (j) Number of SSBP1 puncta normalized to mitochondrial volume (ANOVAs; Tukey HSD). (d, f, h, j) Data points represent individual larvae; data are mean ± SEM. Scale bars = 5 µm. Mitochondrial density = mitochondrial area/cytosolic area.

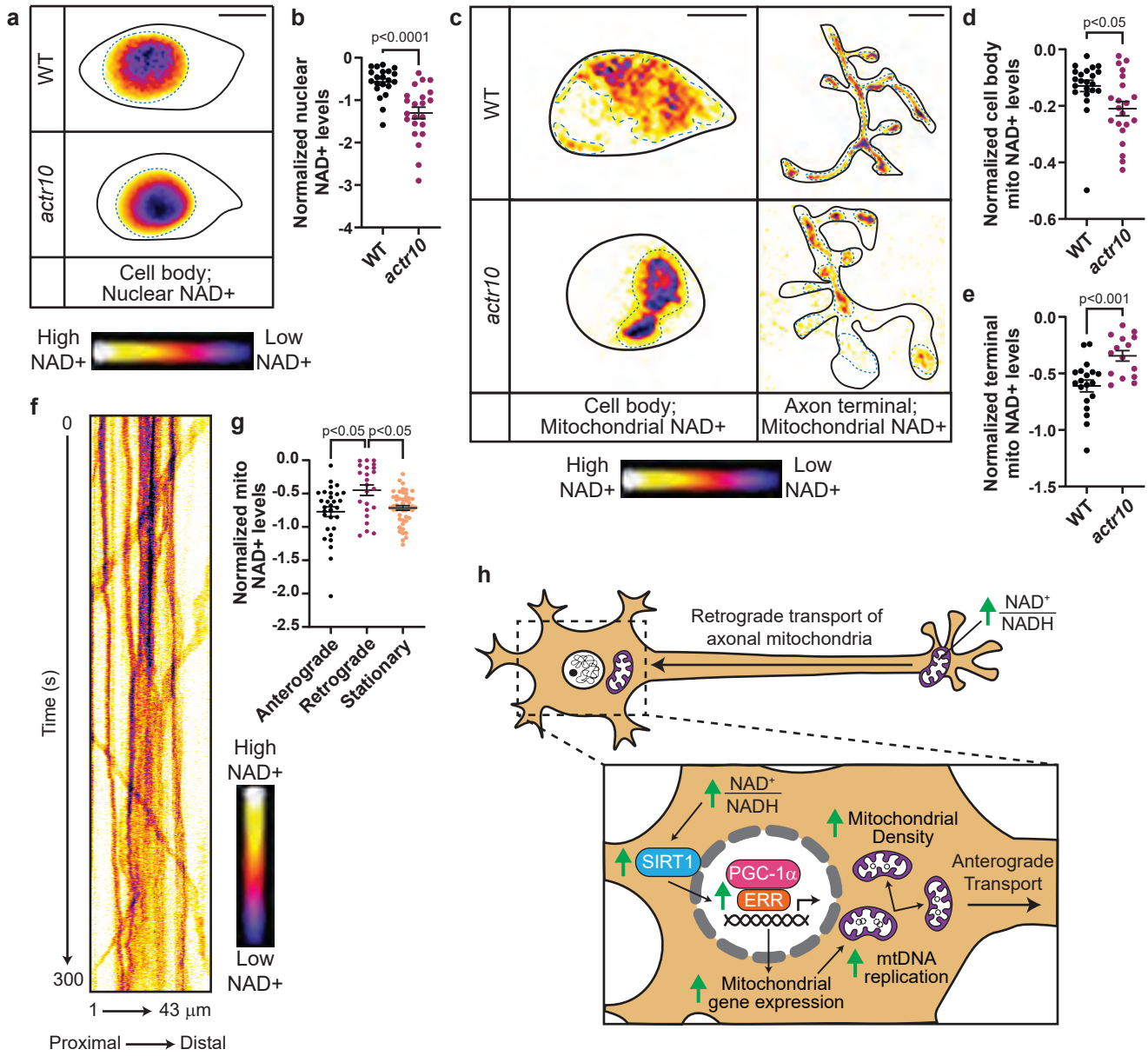

Figure 7: NAD+ levels are altered in *actr10* mutants. (a) pLL cell body expressing a nuclear-localized NAD+ sensor. Black outline surrounds single pLL cell body. Dotted blue outline surrounds nucleus. (c) pLL cell body and axon terminal expressing a mitochondrial matrix-localized NAD+ sensor. Black outline surrounds single pLL cell body and axon terminal. Dotted blue outline surrounds mitochondria. (f) Kymograph of pLL axon expressing a mitochondrial matrix-localized NAD+ sensor. (a, c, f) Inverted heat map indicates levels of NAD+. (b, d, e, g) Mean fluorescence intensity of NAD+ sensor normalized to cytosolic RFP (b, d, e) or mitochondrial matrix-localized TagRFP (g). Data inverted to reflect the direction of change in NAD+ levels as fluorescence intensity decreases in the presence of NAD+ (b, d: Wilcoxon; e: ANOVA; g: Steel-Dwass). (h) Model of mitochondrial retrograde transport regulation of mitochondrial biogenesis. Data are mean ± SEM. (b,d, e) Data points represent individual larvae. (g) Data points represent individual mitochondria from 14 wild type larvae. Scale bars = 5 µm.

386 locks mitochondria with high NAD+ in the axon terminal, blocking this critical signaling step for
387 the positive regulation of mitochondrial biogenesis.

388 **Discussion**

389 Mitochondrial population maintenance is essential for neuronal health and function. These
390 organelles are critical for a variety of functions including ATP production and calcium buffering,
391 particularly in axon terminals [1,2]. Through these functions, mitochondria accrue damage.
392 Damaged organelles must be replaced through the process of mitochondrial biogenesis. Markers
393 of mitochondrial stress such as an increased AMP/ATP or NAD+/NADH ratio as well as
394 increased cellular calcium can activate mitochondrial biogenesis transcriptional programs in the
395 nucleus [3-5,60,76-78]. However, it was unclear how these cellular signals could be transmitted long
396 distances in the neuron to monitor mitochondrial populations in more distal regions of the neuron
397 like the axon terminal. We identified a required role for retrograde return of axonal mitochondria
398 to the cell body to sustain mitochondrial biogenesis transcriptional programs. We show that the
399 return of axonal mitochondria to the cell body stimulates ERR-dependent nuclear gene
400 transcription to regulate expression of mitochondrial genes, mtDNA replication, and ultimately
401 increase mitochondrial biomass in the neuron. This provides a mechanism by which
402 mitochondria in more distal regions of the neuron like the axon terminal can communicate with
403 the nucleus to regulate mitochondrial density and mitochondrial population turnover in neurons.

404 The estrogen-related receptors (ESRRA, ESRRB, and ESRRG) are a family of orphan nuclear
405 receptors first identified due to sequence similarity with estrogen receptors [71,79,80]. The three ERR
406 proteins bind the ERR response element (ERRE) which is found in the promoter of many
407 mitochondrial genes [59,71]. Because of this, increased ERR activity is associated with increased
408 mitochondrial biogenesis in a number of tissues, including neurons [61,62,73,81]. Despite their
409 similarity to estrogen receptors, ERRs do not have the capacity to bind estrogen, but rather are
410 thought to be constitutively active [82]. Their activity can be regulated through expression level,
411 PTMs, or interaction with co-activators like PGC-1α [8,9,81]. PGC-1α regulates ERR transcription
412 and also interacts with ERRs as a coactivator to induce the transcription of mitochondrial
413 biogenesis genes [8,9,62].

414 ERRs serve as mediators between mitochondrial signals and biogenesis transcriptional programs.
415 In non-neuronal cells, signs of mitochondrial depletion or failed health like reduced cellular
416 energy or increased cytosolic calcium have been shown to activate ERR-dependent transcription,
417 either directly or through PGC-1α activation [13,83]. These upstream signals of cellular and
418 mitochondrial health act through enzymes that can directly modify ERR and PGC-1α via PTMs
419 including phosphorylation and acetylation. Two of the most well studied upstream regulatory
420 factors are AMPK and SIRT1, which serve as energy sensors for the cell [6]. AMPK is activated
421 by an increased AMP to ATP ratios and can activate mitochondrial biogenesis through PGC-1α
422 phosphorylation [4,84]. SIRT1 is activated by an increased NAD+ to NADH ratio and can activate
423 mitochondrial biogenesis through PGC-1α and/or ERR de-acetylation [3,67]. AMPK and SIRT1
424 can be artificially activated through AICAR and resveratrol treatment, respectively, to induce
425 mitochondrial biogenesis [64,65,69,84,85]. In our experiments, resveratrol, but not AICAR, treatment
426 was able to rescue *actr10* biogenesis defects, suggesting SIRT1-dependent mitochondrial
427 biogenesis is lost. SIRT1 has been shown to deacetylate human ESRRA at four lysine residues to
428 increase ERRA transcriptional activity[67]. Overexpression of an Esrra mutant mimicking
429 deacetylation at these sites was able to rescue markers of mitochondrial biogenesis in *actr10*
430 mutants, including mitochondrial density and mtDNA replication. Together, this suggests

retrograde transport of axonal mitochondria may stimulate ERR-dependent mitochondrial biogenesis through activation of SIRT1, though we cannot rule out other upstream modulators which could function with SIRT1 in this process.

SIRT1 requires NAD+ as a co-substrate for the removal of acetyl groups from lysines, making NAD+ levels a direct regulator of SIRT1 enzymatic activity [72]. Increased NAD+ levels have been shown to increase SIRT1-mediated de-acetylation of PGC-1α, increasing its transcriptional activity [77,85]. Therefore, local NAD+ levels are a likely signaling mechanism by which non-neuronal cells are able to sense energy levels and respond with transcriptional regulation of mitochondrial biogenesis. However, it was unclear how the predominantly nuclear-localized SIRT1 could sense and respond to levels of NAD+ in mitochondrial populations spread throughout the expansive dendritic and axonal arbors of neurons [86]. Our data suggests that retrograde transport is required to move mitochondria with high levels of NAD+ to the cell body to stimulate biogenesis. We show retrogradely transported mitochondria have higher NAD+ levels and that the NAD+ levels in axon terminal mitochondria are increased when retrograde transport of mitochondria is impeded. We find that failure to return mitochondria with elevated NAD+ levels to the cell body in *actr10* mutants leads to reduced nuclear and cell body mitochondrial NAD+ levels. Based on this, we propose that local SIRT1 activity in the cell body requires increases in the local NAD+ levels which is accomplished by the movement of mitochondria with elevated NAD+ from the axon back to the cell body. Consequent activation of SIRT1 in the cell body then promotes mitochondrial biogenesis through de-acetylation of transcriptional regulators like PGC-1α or ERRs. In support of this, treatment with resveratrol, which circumvents the requirement for NAD+, can rescue mitochondrial density in *actr10* mutant cell bodies. It is likely that additional energy sensing pathways work with NAD+/SIRT1 to control mitochondrial biogenesis through additional transcription factor PTMs. Further work on transcription factor PTMs and associated modulatory pathways will clarify the role of energy sensing through NAD+ and other signaling molecules on the control of mitochondrial biogenesis in neurons.

In conclusion, our work demonstrates that transport of mitochondria from the axon back to the cell body is a positive regulator of neuronal mitochondrial biogenesis through regulation of ERR-dependent gene transcription. Mitochondria derived from biogenesis in the neuronal cell body are critical for maintaining cell body mitochondrial density as well as supplying the anterogradely transported mitochondria that support the axon terminal mitochondrial population. Unsurprisingly, impaired mitochondrial biogenesis can diminish neuronal health and has been linked to diseases like Parkinson's and Alzheimer's diseases [87-90]. However, regulatory mechanisms that govern this critical process in the neuron remain poorly understood. Here we show that neurons in zebrafish larvae require mitochondrial retrograde transport for effective mitochondria-nuclear communication to regulate mitochondrial biogenesis through ERRs. This mechanism provides new insight into how neurons regulate mitochondrial population health and density in response to changing demands on the organelle in distal compartments.

Acknowledgments: We would like to acknowledge members of the Drerup lab and Dr. Samantha Lewis for thoughtful discussions of the work and critique of the manuscript. The constitutively active KIF1A motor domain construct was provided by Dr. Marvin Bentley. We would like to thank the University of Wisconsin Carbone Cancer Center Flow Cytometry Laboratory, supported by P30 CA014520, for use of its facilities and assistance with fluorescence activated cell sorting. We would like to thank Randall Massey and the University of

Wisconsin School of Medicine and Public Health Electron Microscopy Facility for assistance with Transmission Electron Microscopy.

Funding:

National Institutes of Health grant R01NS124692 (CMD)

National Science Foundation grant DEG-2137424 (AEL)

National Institutes of Health grant T32GM007133 (University of Wisconsin-Madison Predoctoral Training Program in Genetics; AEL)

University of Wisconsin-Madison Office of the Vice Chancellor for Research (CMD)

Wisconsin Alumni Research Foundation (CMD)

Author Contributions:

Conceptualization: AEL, CMD

Data acquisition and analysis: AEL, CS, RS, CMD

Funding acquisition: AEL, CMD

Writing – original draft: AEL

Writing – review & editing: CMD

Competing interests: The authors declare no competing interests.

Data and materials availability: All data and materials are available upon request from the corresponding author.

Materials and Methods

Zebrafish husbandry

All zebrafish (*Danio rerio*) work was done in accordance with the University of Wisconsin-Madison Institutional Animal Care and Use Committee guidelines. Adult zebrafish were kept at 28°C and embryos were spawned according to established protocols [91]. Embryos and larvae were kept in embryo media (995 µM MgSO4, 154 µM KH2PO4, 42 µM Na2HPO4, pH 7.2, 1.3 mM CaCl2, 503 µM KCl, 15 mM NaCl, 714 µM NaHCO3), maintained at 28°C, and developmentally staged using established methods [92]. All experiments were performed at 4 dpf unless otherwise specified. Sex is not determined at this stage. Zebrafish strains used for these experiments are listed in Table 1. The Tg(*hsp70l:EGFP-en.sill*)^{uwd12} transgenic was derived using Tol2-mediated transgenesis and the *hsp70:eGFP-SILL* plasmid as described [93]. Genotyping for *actr10*^{nl15} [35], *p150a*^{y625} [37], *p150b*^{nl16} [35], and *nudc*^{nl21} [42] was done as previously described using the primers in Table 2.

Cloning

The DNA expression plasmids used in this paper are listed in Table 1. Novel DNA expression constructs were constructed using Gateway cloning[93] or Gibson cloning with oligonucleotides listed in Table 2 [94]. *5kbneurod:POLG2-GFP-p2a-mitoTagRFP* was created from a human POLG2-GFP template plasmid[12,46]. *5kbneurod1:kif1a-egfp-omp25* ["MitoTruck"] was created using the zebrafish outer membrane protein 25 (OMP25) mitochondrial localization sequence (MLS) cloned from 4 dpf zebrafish cDNA. The truncated constitutively active rat ortholog of KIF1A was cloned from *pBA-kif1a393-tdTomato-FKBP* [95]. *5kbneurod1:cox8a-cox8a-halotag* was created by fusing two copies of the cox8a MLS to a HaloTag. *5kbneurod1:esrra-p2a-mRFP* was created using the zebrafish *esrra* sequence derived from 4 dpf zebrafish cDNA and existing

517 p2a and mRFP plasmids[93]. Esrra^{4KR} expression plasmid was created using consecutive site-
518 directed mutagenesis reactions with the Agilent QuikChange Lightning Site-Directed
519 Mutagenesis Kit. Lysines at amino acid 129, 138, 160, and 162 in the zebrafish ortholog of Esrra
520 were converted to arginines. *5kbneurod1:cox8a-cox8a-NAD-p2a-RFP* was created from
521 plasmids containing a double cox8a MLS, a NAD+ biosensor (Addgene plasmid 186791; [96]) and
522 a p2a-RFP. *5kbneurod1:H2B-NAD-p2a-RFP* and *5kbneurod1:cox8a-cox8a-NAD-p2a-*
523 *mitoTagRFP* were created from the *5kbneurod1:cox8a-cox8a-NAD-p2a-RFP* plasmid and either
524 a plasmid containing an H2B nuclear localization signal or a p2a-mitoTagRFP.The NAD+
525 biosensor consists of a circularly permuted Venus fluorescent protein (cpVenus) with a bipartite
526 NAD+-binding domain modeled from bacterial DNA ligase [96]. *5kbneurod1:cox8a-cox8a-*
527 *paGFP-p2a-mitoTagRFP* was created from plasmids containing a double cox8a MLS, a photo-
528 activatable GFP, and a p2a-mitoTagRFP. *hsp70l:EGFP-en.sill* was created using existing
529 plasmids containing the hsp70 minimal promotor, eGFP, and the 3' SILL enhancer element that
530 limits expression to the pLL ganglion [93,97]. *hsp70l:POLG2-GFP-p2a-mitoTagRFP* was created
531 from the *5kbneurod:POLG2-GFP-p2a-mitoTagRFP* plasmid and the hsp70 minimal promoter.
532 For all expression plasmids except the *hsp70* driven constructs, expression was controlled by a
533 5kb portion of the *neurod* promotor as previously described [93,98]. All novel DNA expression
534 plasmids were sequenced and verified prior to use.

535 Live imaging acquisition and analysis

536 For live imaging of pLL neurons, we used a combination of transient transgenesis and stable
537 transgenic expression. For transient transgenesis, 3-25 pg of plasmid DNA was microinjected
538 into zebrafish zygotes as previously described [35,99,100]. Plasmids used for these experiments are
539 listed in Table 1. For imaging, zebrafish larvae were sorted to identify larvae with expression in a
540 subset of pLL neuron cell bodies using an AxioZoom V.16 Zeiss microscope. For HaloTag
541 constructs, larvae were treated with Janelia Fluor 635 in embryo media at 1 μM for 1-2 h or 0.1
542 μM overnight at 28.5°C in the dark. For all live imaging, larvae were anesthetized in 0.02%
543 tricaine, mounted in 1.5% low melt agarose in embryo media, and imaged with an Olympus
544 FV3000 confocal microscope with a 40x (NA 1.25) silicone oil objective. Optimal interslice
545 interval was used for all imaging.

546 Larval TgBAC(*neurod:egfp*)^{nl1} (Fig. 1a) and *Tg(hsp70:eGFP-SILL)*^{uwd12Tg} (Supplementary Fig.
547 1a) transgenic zebrafish images were created by stitching overlapping regions of the larvae
548 imaged using the Olympus FV3000 with a 10X objective using the pairwise stitching plugin in
549 ImageJ [101,102]. Non-linear adjustment to midtones to show the full nervous system was done
550 using the levels function in Adobe Photoshop. For TgBAC(*neurod:egfp*)^{nl1}, a brightfield image
551 of the full larva was taken using the AxioZoom V.16 Zeiss microscope with a Zeiss Axio 506
552 color camera and overlaid using Adobe Photoshop with opacity adjusted to 10%. For
553 *Tg(hsp70:eGFP-SILL)*^{uwd12Tg}, brightfield images from the Olympus FV3000 were stitched and
554 overlaid with an opacity of 30%.

555 To quantify mitochondrial density in the pLL cell body and axon terminal, area was measured
556 from standard deviation z-projections in ImageJ. Mitochondrial area was measured using a
557 manually applied threshold while cytosolic area was measured by manual tracing or applied
558 threshold of a cytosolic fill. Mitochondrial density was calculated as mitochondrial area divided
559 by cytosolic area. To quantify mitochondrial or cell volume, the 3D objects counter was used in
560 ImageJ using a manually applied threshold [102].

561 For POLG2 axon terminal analysis, *5kbneurod:POLG2-GFP-p2a-mitoTagRFP* was transiently
562 expressed in pLL neurons by zygotic microinjection as described [100] and terminal regions were
563 imaged as described above. POLG2+ puncta were manually counted and mitochondrial volume
564 was quantified as described above.

565 Mitochondrial axonal transport analyses were done as described previously [100]. Briefly, transient
566 transgenesis of *5kbneurod1:mitotagRFP* was used to visualize mitochondria in pLL axons. 30–
567 100 µm lengths of axon were imaged as a single *z*-plane at a rate of 300 ms per frame for 1000
568 frames. Kymographs were generated using the ImageJ Multi Kymograph function [102].
569 Anterograde, retrograde, and bidirectional mitochondria number were quantified using
570 kymographs while stationary mitochondria number was quantified by visual analysis of transport
571 videos. Mitochondrial length was manually measured from transport movies using the line
572 selection tool in ImageJ.

573 For NAD+ quantification, NAD sensor constructs were transiently expressed in pLL neurons by
574 zygotic microinjection. For single timepoint imaging, larvae were mounted live as described
575 above and cell body and axon terminal regions were imaged at 4 dpf with consistent laser power
576 and detector gain for all images. Transport analysis was done as described above with sequential
577 imaging of cpVenus and RFP channels[35,100]. For cell body and axon terminal mitochondria
578 analysis (*5kbneurod1:cox8a-cox8a-NAD-p2a-RFP*), cell body and axon terminal regions were
579 isolated using the mRFP cytosolic signal as a mask and the image subtraction function in ImageJ
580 [102]. cpVenus and mRFP mean fluorescence intensity were then quantified from sum projections
581 of the isolated region. For nuclear analysis (*5kbneurod1:H2B-NAD-p2a-RFP*), sum projections
582 were created for cpVenus and mRFP. Nuclear cpVenus mean fluorescence intensity was
583 quantified by manual outlining of nucelar area. mRFP mean fluorescence intensity was
584 quantified by manual outlining of cytosolic area. For transport analysis (*5kbneurod1:cox8a-*
585 *cox8a-NAD-p2a-mitoTagRFP)*, mitochondria were identified as moving anterogradely,
586 retrogradely, or stationary by visual analysis of transport videos. cpVenus and RFP mean
587 fluorescence intensity were quantified by manual outlining of individual mitochondria. For all
588 analyses, mean fluorescence intensity of cpVenus was normalized to mean fluorescence intensity
589 of RFP to control for differences in expression level. NAD+ binding to the bipartite NAD+-
590 binding domain in the biosensor decreases cpVenus fluorescence intensity in a dose-dependent
591 manner [96]. The images in Figure 7 were generated using the fire lookup table in ImageJ and the
592 images/data are inverted to appropriately reflect the direction of change in NAD+ levels.

593 <u>Drug treatment</u>

594 Resveratrol and AICAR (5-aminoimidazole-4-carboxamide ribonucleotide) stocks (200 mM and
595 27.5 mM respectively) were diluted in embryo media to concentrations previously shown to be
596 effective in larval zebrafish (Resveratrol 300 µM, AICAR 1 mM; [70]). At 3 dpf, transient
597 transgenic larval zebrafish expressing cytosolic GFP and mitochondrially localized tagRFP (see
598 Table 1 for DNA constructs) were placed in a 6 well plate and incubated overnight (18-24 h) in
599 drug or equal amount of drug solvent (DMSO for resveratrol, sterile H_2O for AICAR) in embryo
600 media. After treatment, larvae were mounted live, pLL neuronal cell bodies were imaged, and
601 mitochondrial density analyzed as described above.

602 <u>Heat shock-induced expression of Drp1^{K38A} and POLG2-GFP</u>

603 For DRP-1 analysis, *Hsp701:Drp1K38A-mRFP* [35] or *5kbneurod1:RFP* [35] (control) was
604 transiently expressed with *5kbneurod1:mito-eGFP* in pLL neurons by zygotic microinjection as
605 described [100]. At 4 dpf, larvae of both groups were placed in PCR strip tubes (2-3 larvae per tube)

606 with approximately 200 µl of embryo media. Larvae were incubated at 37°C for 1 hour in a PCR
607 machine (BioRad) then returned to 28°C. Larvae were fixed in 4% paraformaldehyde 7 hours
608 post-heat shock for subsequent HCR RNA FISH or immunolabeling as described below.

609 For POLG2-GFP cell body puncta analysis, *Hsp701:POLG2-GFP-p2a-mitoTagRFP* was
610 transiently expressed in pLL neurons by zygotic microinjection as described [100]. At 4 dpf,
611 embryo media was pre-heated to 37°C in 50 mL conical tubes. Larvae were transferred to the
612 pre-heated embryo media in 50 mL conical tubes and kept at 37°C for 1 hour. Larvae were then
613 returned to 28°C media. Larvae were fixed in 4% PFA/0.25% Triton X-100 7 hours post-heat
614 shock for subsequent imaging. Fixed larvae were mounted between glass slides and #1.5
615 coverslip with Fluoromount mounting medium prior to imaging with an Olympus FV3000
616 confocal microscope with a 60x (NA1.42) oil objective. Punctal quantification was done as
617 described above for axon terminals.

618 Nuclear localization analysis

619 *5kbneurod1:mRFP-esrra* or *5kbneurod1:mRFP-esrra*^{4KR} was transiently expressed in pLL
620 neurons by zygotic microinjection as described [100]. At 4 dpf, larvae were fixed in 4% PFA/0.25%
621 Triton X-100 and co-incubated with DAPI (1:500) at 4°C overnight. Larvae were imaged as
622 described above for cell body POLG2-GFP. DAPI was used to mask out nuclear RFP signal.
623 Mean fluorescence intensity was then quantified from sum projections of the nuclear and
624 cytosolic regions.

625 Photolabeling

626 *5kbneurod1:cox8a-cox8a-paGFP-p2a-mitoTagRFP* was transiently expressed in pLL neurons by
627 zygotic microinjection as described [100]. Cell body or axon terminal mitochondrial-matrix
628 localized PA-GFP was specifically photoactivated by illuminating with a 405 nm laser using a
629 region of interest (ROI) defined around the structure. For each larva, a pre-activation image was
630 taken (488 nm and 561 nm lasers), the region was scanned for 1 to 5 seconds with 1% 405 nm
631 laser power using the stimulation function for conversion, and a post-activation image (488 nm
632 and 561 nm lasers) was taken to confirm activation. The axon terminal was then re-imaged at set
633 timepoints post-conversion. Due to transient expression, PA-GFP was not expressed in every
634 axon terminal. To reduce variability due to differences in axon length, only axon terminals
635 innervating sensory organs in the center of the trunk (neuromasts 2, 3, or 4) were used for
636 analysis. PA-GFP and MitoTagRFP mitochondrial area were quantified as described earlier.
637 "Proportion original mitochondria" for terminal activation and "proportion of cell body-derived
638 mitochondria" for cell body activation was quantified as PA-GFP area/MitoTagRFP area (see
639 Figure S3).

640 Photoconversion of mitochondrially localized mEos was performed using the stable transgenic
641 *Tg(-5kbneurod1:mito-mEos)*^{y586Tg} as previously described [37]. The pLL ganglion was specifically
642 converted by illuminating with a 405 nm laser through a z-stack of the entire ganglion with
643 regional restriction using a region of interest (ROI) defined around this structure. For each larva,
644 a preconversion image was taken (488 nm and 561 nm lasers), the stack was scanned with 1%
645 405 nm laser power for conversion, and a postconversion image (488 nm and 561 nm lasers) was
646 taken to confirm complete green to red conversion of mEos in pLL cell bodies. For 4 hour
647 timepoint analysis, the axon terminal of a sensory organ in the center of the trunk (NM3) was
648 imaged 4 hours post pLL ganglion conversion. All microscope settings were kept consistent for
649 all images. For axon terminal analysis, the red and green channels were merged and a mask was
650 created by thresholding a standard deviation projection of the axon terminal *z*-stack. The mask

651 was applied to a sum projection of the red channel and mean fluorescence was quantified. For
652 timelapse analysis, a z-stack through an ROI surrounding NM3 was scanned minute for 6 hours.
653 Image analysis was performed by manually scanning through standard deviation z-stack
654 projections from the time series. Cell body derived (red photoconverted) mitochondria were
655 counted and volume measured using the 3D objects counter in ImageJ.

656 In situ Hybridization and Hybridization Chain Reaction RNA Fluorescent In situ Hybridization
657 (HCR RNA FISH)

658 Colorimetric in situ hybridization was done according to established protocols [99,103]. To generate
659 probes for *in situ* hybridization, we amplified 200-600 base pair regions of relevant cDNA within
660 the open reading frames of genes of interest to use as a template for probe synthesis ([104]; Table
661 2). Zebrafish were fixed overnight in 4% paraformaldehyde (PFA) in phosphate-buffered saline
662 (PBS) at 4°C. Fixed larvae were washed in PBS/0.1% Tween-20 and dehydrated in a methanol
663 series. Larvae were stored in methanol at -20°C. Larvae were rehydrated with PBS/0.1% Tween-
664 20 in a reverse methanol series. Larvae were treated with 10 µg/ml proteinase K in PBS/0.1%
665 Tween-20 for 15 minutes then immediately fixed for 20 min in 4% PFA at room temperature
666 (RT). Larvae were washed with PBS/0.1% Tween-20 then prehybridized for 1-2 hours at 65°C.
667 Larvae were incubated overnight at 65°C with probe diluted 1:200 in hybridization buffer (10
668 mM citric acid, 0.1% Tween-20, 50 µg/ml heparin, 5× saline sodium citrate (SSC), 50%
669 formamide). Larvae were washed at 65°C with a hybridization buffer-SSC buffer series (2:1
670 buffer:2x SSC 15 min; 1:2 buffer:2x SSC 15 min; 2x SSC 15 min; 0.2x SSC 30 min twice).
671 Larvae were then washed at RT with 2:1 and then 1:2 0.2x SSC:PBS/0.1% Tween-20 for 5 min.
672 Larvae were blocked in block solution (2% goat serum, 10% bovine serum albumin in PBS/0.1%
673 Tween-20) for 2 hours at RT, and then sheep anti-digoxigenin (1:10,000) in block solution
674 overnight at 4°C. Larvae were washed 6 times 15 min in PBS/0.1% Tween-20, 3 x 5 min in
675 coloration buffer (100 mM Tris–HCl pH 9.5, 50 mM MgCl2, 100 mM NaCl, 0.1% Tween-20),
676 then stained with 0.45% nitro blue tetrazolium, 0.35% 5-bromo-4-chloro-3-indolyl phosphate in
677 a coloration buffer in dark until color development. Larvae were washed with PBS/0.1% Tween-
678 20, fixed for 20 min in 4% PFA at RT, dehydrated in a methanol series, and rehydrated for
679 imaging and sorting of RNA expression. WT and *actr10* mutant zebrafish were kept in the same
680 tube for processing, then blindly sorted based on RNA expression into two groups (high and low
681 expressing). Representative larvae were mounted in 1.5% low melt agarose in embryo media and
682 imaged with a Zeiss Axio Imager.M2 microscope with Zeiss Axio 506 color camera. Sorted
683 larvae were genotyped using the oligonucleotides in Table 2.

684 HCR RNA FISH was performed as described previously [51]. An mRNA transcript-specific probe
685 set for each gene of interest was designed by Molecular Instruments (Table 3). Larvae fixation,
686 methanol dehydration/rehydration, and Pro K treatment were performed as described for
687 colorimetric in situ hybridization with modification in the Pro K treatment for larvae less than 4
688 dpf. 2 dpf larvae were treated with Pro K for 5 min, 3 dpf for 10 min, and 4 dpf for 15 min,
689 followed by post-fixation. Larvae were incubated with a manufacturer-supplied hybridization
690 buffer at 37°C for 1 h and then incubated in 4 nM (*pgc1a* and *tfam*) or 16 nM (others) probe in
691 hybridization buffer at 37°C overnight. Larvae were washed with a manufacturer-supplied wash
692 buffer and then SSC/0.1% Tween-20. Then, larvae were incubated in a manufacturer-supplied
693 amplification buffer at RT for 30 min, during which manufacture-supplied reporter-labeled
694 fluorescent hairpins were individually heated at 95°C and then cooled to RT for 30 min in the
695 dark. Larvae were placed in fresh amplification buffer with 60 nM hairpins. B1 probes were
696 labeled with 546 nm wavelength hairpins while B2 probes were labeled with 647 nm wavelength

697 hairpins combined in the same tube. Larvae were incubated overnight in the dark at RT. Larvae
698 were mounted between glass slides and #1.5 coverslip with Fluoromount mounting medium prior
699 to imaging with an Olympus FV3000 confocal microscope with a 60x (NA1.42) oil objective.
700 For each probe, laser power and detector gain were kept consistent for all images.

701 To quantify HCR signal in the whole pLL ganglion in *TgBAC(neurod:eGFP)*^{nl1} larvae, a mask
702 was created using the GFP channel threshold using the default auto thresholding algorithm in
703 ImageJ and the image subtraction function was used to remove non-neuronal signal. After using
704 the mask to exclude signal outside the pLLg, a sum projection of the probe signal was created
705 and mean fluorescence intensity was measured. To quantify HCR signal in single cell bodies, a
706 substack was created around the cell of interest and a sum intensity z-projection of the probe
707 signal was created. The cell body was manually outlined and mean fluorescence intensity of the
708 probe signal within the cell body was measured. To quantify background signal, a region outside
709 the pLLg or cell body was selected and the sum intensity of probe signal was measured.
710 Background mean signal was subtracted from pLL mean signal to get the normalized mean
711 fluorescence intensity.

712 Immunolabeling

713 For SSBP1 and TFAM immunolabeling, transient transgenesis of either *5kbneurod1:mito-eGFP*
714 or *5kbneurod1:mitotagRFP* was used to localize pLL cell body mitochondria. Larvae were fixed
715 in 4% PFA/0.25% Triton X-100 at 4°C overnight then incubated in water at RT overnight.
716 Larvae were kept in block (0.1% Triton X-100, 1% dimethyl sulfoxide, 0.02% sodium azide,
717 0.5% bovine serum albumin, 5% goat serum) at RT for 2h, then incubated with antibody in block
718 overnight at 4°C. Antibodies were validated by western blot (Supplementary Fig. 1m). Larvae
719 injected with *5kbneurod1:mito-eGFP* were incubated with chicken anti-GFP (1:2000) to amplify
720 signal. Larvae were incubated with either rabbit anti-SSBP1 (1:500) or rabbit anti-TFAM
721 (1:100). Larvae were then washed in PBS/0.1% Triton X-100 before incubation in goat anti-
722 chicken AlexaFluor 488 (1:1000) and goat anti-rabbit AlexaFluor 568 (1:1000) or goat anti-
723 rabbit AlexaFluor 647 (1:1000) at 4°C overnight. Larvae were washed in PBS/0.1% Triton X-
724 100 prior to imaging as described for HCR. For analysis, a mask was created from the
725 mitochondrial channel using the default auto thresholding algorithm in ImageJ and the image
726 subtraction function was used to remove signal outside the pLL cell body. For TFAM
727 quantification, the 3D objects counter function in ImageJ and manual thresholding was used to
728 quantify volume of TFAM puncta and mitochondria (mitochondrial volume used for
729 normalization). For SSBP1 quantification, SSBP1 puncta were manually counted and normalized
730 to mitochondrial volume.

731 Transmission Electron Microscopy

732 4 dpf wild type and *actr10* mutant larvae samples were dissected by removing the trunks
733 posterior to the pLLg and then fixed in Karnovsky's fixative (2.5% glutaraldehyde/2.0%
734 formaldehyde in 0.1M NaPO4 buffer (PB), pH=7.2) at 4°C overnight. All remaining steps were
735 performed on the specimens in glass scintillation vials on a rotator unless specified. The fixative
736 was removed and the samples washed 5 x 5 min in PB at RT. Post-fixation was performed on the
737 samples in 1% OsO4 in PB for 1 hour at RT. The samples were again washed in PB, 7 x 5
738 minutes at RT. Dehydration was performed with a graded series of EtOH (35%, 50%, 70%,
739 80%, 90% 5 x 5 minutes, 95% for 10 minutes, 100% for 3 x 10 minutes) at RT. Specimens were
740 transitioned from EtOH by rinsing 2 x 7 minutes in acetone at RT. Samples were infiltrated and
741 embedded in EMBed 812 resin (EMS Hatfield; PA 19440) using a graded series of 2:1 Acetone /

742 EMBed812 1 hour RT, 1:1 Acetone / EMBed812 overnight RT, 1:2 Acetone / EMBed812 2
743 hours RT. 100% EMBed 812 resin infiltrations continued in uncapped vials for 1 hour at 65ºC in
744 a laboratory microwave, with a fresh change of resin for 1 hour at 75ºC. Final embedding was
745 done in EMBed 812 resin in aluminum weighing dishes placed in a 60ºC drying oven and
746 allowed to polymerize for 2 days. Polymerized samples had the aluminum dishes stripped, with
747 the target specimen area sawed out with a jewelers saw and glued to blank polymerized stubs of
748 EMBed 812 resin. Specimens were sectioned on a Reichert-Jung Ultracut E ultra-microtome
749 with sections collected on formvar coated, Cu 2x1 slot grids. Grids were post-stained in uranyl
750 acetate and Reynolds lead citrate and viewed on a Philips CM120 at 80kV. Images were
751 collected on a BioSprint12 digital camera. One section of the pLLg was imaged for a WT and
752 *actr10* mutant larvae. All cells visible within the section were analyzed. Images were calibrated
753 in ImageJ and analyzed by manual counting of mitochondria and manual outlining for
754 mitochondrial, cell, and nuclear area. Cytosolic area was calculated as cell area minus nuclear
755 area.

756 Western blot

757 Western blot of TFAM and SSBP1 protein was done as described previously [35]. Protein lysates
758 of 4 dpf wildtype larvae were run on a 12% sodium dodecyl sulfate polyacrylamide
759 electrophoresis gel. After transfer to the polyvinylidene difluoride membrane, the blots were
760 blocked in 5% nonfat dry milk in 1X PBS/0.1% Tween for 1–4 hours before incubation with
761 anti-TFAM (1:1000) or anti-SSBP1 (1:500) overnight in block at 4°C. Membranes were then
762 washed in 1X PBS, 0.1% Tween20 and incubated with secondary antibody conjugated to
763 horseradish peroxidase for 90 min at RT. The blot was developed with a Western Sure
764 Chemiluminescent Substrate (LiCor) on a C-DiGit Blot Scanner.

765 Embryo dissociation and fluorescence activated cell sorting (FACS)

766 20-30 4 dpf *Tg(hsp70:eGFP-SILL)*^{uwd12} larvae were collected in 1.5 ml microcentrifuge tubes.
767 Embryo media was removed and larvae were incubated in 100 µL sterile, calcium-free ringer's
768 solution (116 mM NaCl, 2.6 mM KCl, 5 mM HEPES pH 7.0) at RT for 5 min. 600 µL of sterile
769 protease solution (0.25% trypsin, 1 mM EDTA, pH 8.0, PBS) was warmed to 28°C and 27 µl of
770 Collagenase P (100 mg/mL in HBSS) was added to the tube and mixed. Larvae were incubated
771 at 28°C. Every 30s, larvae were homogenized for 30s by pipetting first with a P1000 pipette until
772 partially dissociated, then with a P200 pipette until fully dissociated. Once dissociated, 100 µl of
773 sterile stop solution (30% calf serum, 6 mM CaCl2, PBS) was added and mixed. The cells were
774 spun down at 350xg at 4°C for 5 min. The supernatant was removed and replaced with 500 µl
775 sterile suspension solution (1% FBS, 0.8 mM CaCl2, 50 U/mL penicillin, 0.05 mg/mL
776 streptomycin, DMEM) chilled to 4°C. Cells were spun at 350xg at 4°C for 5 min. The
777 supernatant was removed and 500 µl of chilled sterile suspension solution was used to resuspend
778 cells. Resuspended cells were passed through a 40 µm cell strainer into FACS tube and stored on
779 ice until sorting. Immediately prior to sorting, DAPI (1:1000) was added to sort out dead cells.
780 GFP+ DAPI- cells were sorted on a BD FACSAria™ III Cell Sorter with a 100 µm nozzle into
781 500 µL TRIzol LS in a 1.5 mL microcentrifuge tube.

782 Bulk RNA sequencing and analysis

783 Sorted pLL neurons were pooled into 3 replicates each for wild type and *actr10* samples. RNA
784 was isolated using TRIzol. The SMART-Seq® v4 Ultra® Low Input RNA Kit was used for
785 poly(A)+ selection, cDNA synthesis and amplification, followed by Illumina 150-bp paired-end

786 sequencing performed by Azenta Life Sciences (South Plainfield, NJ). Sequence reads were
787 trimmed to remove possible adapter sequences and nucleotides with poor quality using
788 Trimmomatic v.0.36 [105]. The trimmed reads were mapped to the Danio rerio GRCz10.89
789 reference genome available on ENSEMBL using the STAR aligner v.2.5.2b [106]. Unique gene hit
790 counts were calculated by using FeatureCounts from the Subread package v.1.5.2 [107]. Only
791 unique reads that fell within exon regions were counted. Using DESeq2 [108], a comparison of
792 gene expression between WT and *actr10* samples was performed. The Wald test was used to
793 generate p-values and log2 fold changes. Genes with an adjusted p-value < 0.05 and absolute
794 log2 fold change > 1 were called as differentially expressed genes for each comparison.
795 Alignment and differential expression analysis was performed by Azenta Life Sciences (South
796 Plainfield, NJ).

797 KEGG pathway enrichment was performed for genes that were called as significantly
798 upregulated or significantly downregulated using the ShinyGO (v0.82) webserver (*84-86*). *Danio*
799 *rerio* gene IDs were used as input and background genes were defined as all genes that were
800 detectable in the RNA-sequencing dataset. Default parameters were maintained. KEGG pathway
801 plots were downloaded directly from the ShinyGO webserver. Gene Set Enrichment Analysis
802 (GSEA) for differentially expressed genes was performed using the clusterProfiler R package
803 with all gene ontology terms included, using the genome-wide annotation for Zebrafish
804 (org.Dr.eg.db v3.19.1; [109]). Zebrafish gene IDs were converted to their closest human gene
805 orthologues using the g:Profiler g:Orth webserver [110]. Fisher's exact test enrichment analysis was
806 performed using the fisher.test function in R to test overlap between significantly upregulated or
807 significantly downregulated genes and either the MitoCarta database or the ESRRG ChipSeq
808 targets [49,63]. Transcription factor enrichment analysis was performed using the TFEA.ChIP
809 webserver which uses information derived from the ChIP-seq datasets available from the
810 ENCODE project, GEO Datasets, GeneHancer, ReMap 2018, and ReMap 2022 databases [111].
811 The significantly downregulated genes were used with background genes defined as all genes
812 that were detectable in the RNA-sequencing dataset. Wilcoxon rank-sum was used for
813 transcription factor ranking. Over-representation analysis of transcription factor target motifs
814 was performed using the Webgestalt webserver with the functional database identified as
815 ''network: transcription factor target" [112]. The significantly downregulated genes were used with
816 background genes defined as all genes that were detectable in the RNA-sequencing dataset.
817 Default parameters were maintained. Volcano plots of differentially expressed genes and
818 transcription factor enrichment were created using the ggplot2 R package [113].

819 <u>Experimental design, statistical analysis, and figure assembly</u>

820 All image analysis was performed using ImageJ [102]. Statistical analysis was performed using
821 JMP18 and data plots made using GraphPad Prism 10, unless indicated otherwise in the method
822 section. Sample size estimated based on previous work and determined by power analyses.
823 Imaging and analysis done blind to genotype, allowing inherent randomization and blinding to
824 experimental condition. All experiments were replicated no less than two times (experimental
825 replicates) with sample size for each experiment representing biological replicates. Statistical
826 tests/post hoc analyses and other statistical details for each data set are indicated in the text or
827 figure legends. For parametric data, ANOVAs were used with Tukey HSD post-hoc contrasts for
828 multiple pairwise comparisons within a dataset. For nonparametric data, single comparisons
829 were done using Wilcoxon/Kruskal-Wallis analysis, multiple comparisons using the Steel-Dwaas
830 test. Images were created using ImageJ and linear adjustments to brightness/contrast were made

equally for images being compared. Figures were compiled in Adobe Illustrator and supplemental movies were handled in Adobe After Effects.

References

1. Suomalainen, A., and Nunnari, J. (2024). Mitochondria at the crossroads of health and disease. Cell *187*, 2601-2627. 10.1016/j.cell.2024.04.037.
2. Misgeld, T., and Schwarz, T.L. (2017). Mitostasis in Neurons: Maintaining Mitochondria in an Extended Cellula r Architecture. Neuron *96*, 651-666. 10.1016/j.neuron.2017.09.055.
3. Gerhart-Hines, Z., Rodgers, J.T., Bare, O., Lerin, C., Kim, S.-H., Mostoslavsky, R., Alt, F.W., Wu, Z., and Puigserver, P. (2007). Metabolic control of muscle mitochondrial function and fatty acid oxid ation through SIRT1/PGC-1α. The EMBO Journal *26*, 1913-1923. 10.1038/sj.emboj.7601633.
4. Jäger, S., Handschin, C., St.-Pierre, J., and Spiegelman, B.M. (2007). AMP-activated protein kinase (AMPK) action in skeletal muscle via dire ct phosphorylation of PGC-1α. Proceedings of the National Academy of Sciences *104*, 12017-12022. 10.1073/pnas.0705070104.
5. Ojuka, E.O., Jones, T.E., Han, D.H., Chen, M., and Holloszy, J.O. (2003). Raising Ca 2+ in L6 myotubes mimics effects of exercise on mitochondrial biogenesis in muscle. The FASEB Journal *17*, 675-681. 10.1096/fj.02-0951com.
6. Cantó, C., Gerhart-Hines, Z., Feige, J.N., Lagouge, M., Noriega, L., Milne, J.C., Elliott, P.J., Puigserver, P., and Auwerx, J. (2009). AMPK regulates energy expenditure by modulating NAD+ metabolism and SIRT1 activity. Nature *458*, 1056-1060. 10.1038/nature07813.
7. Scarpulla, R.C. (2011). Metabolic control of mitochondrial biogenesis through the PGC-1 family regulatory network. Biochimica et Biophysica Acta (BBA) - Molecular Cell Research *1813*, 1269-1278. 10.1016/j.bbamcr.2010.09.019.
8. Schreiber, S.N., Emter, R., Hock, M.B., Knutti, D., Cardenas, J., Podvinec, M., Oakeley, E.J., and Kralli, A. (2004). The estrogen-related receptor α (ERRα) functions in PPARγ coactivator 1α (PGC-1α)-induced mitochondrial biogenesis. Proceedings of the National Academy of Sciences *101*, 6472-6477.10.1073/pnas.0308686101.
9. Schreiber, S.N., Knutti, D., Brogli, K., Uhlmann, T., and Kralli, A. (2003). The Transcriptional Coactivator PGC-1 Regulates the Expression and Act ivity of the Orphan Nuclear Receptor Estrogen-Related Receptor α (ERRα). Journal of Biological Chemistry *278*, 9013-9018. 10.1074/jbc.M212923200.
10. Virbasius, J.V., and Scarpulla, R.C. (1994). Activation of the human mitochondrial transcriptionfactor A gene by nuclear respiratory factors: a potential regulatory linkbetween nuclear and mitochondrial gene expression in organellebiogenesis. Proceedings of the National Academy of Sciences *91*, 1309-1313. 10.1073/pnas.91.4.1309.
11. Kleele, T., Rey, T., Winter, J., Zaganelli, S., Mahecic, D., Perreten Lambert, H., Ruberto, F.P., Nemir, M., Wai, T., Pedrazzini, T., and Manley, S. (2021). Distinct fission signatures predict mitochondrial degradation or biogenesis. Nature *593*, 435-439. 10.1038/s41586-021-03510-6.
12. Lewis, S.C., Uchiyama, L.F., and Nunnari, J. (2016). ER-mitochondria contacts couple mtDNA synthesis with mitochondrial division in human cells. Science *353*, aaf5549. 10.1126/science.aaf5549.

13. Cardanho-Ramos, C., and Morais, V.A. (2021). Mitochondrial Biogenesis in Neurons: How and Where. International Journal of Molecular Sciences *22*, 13059. 10.3390/ijms222313059.
14. Davis, A.F., and Clayton, D.A. (1996). In situ localization of mitochondrial DNA replication in intact mammalian cells. Journal of Cell Biology *135*, 883-893. 10.1083/jcb.135.4.883.
15. Schultz, R.A., Swoap, S.J., McDaniel, L.D., Zhang, B., Koon, E.C., Garry, D.J., Li, K., and Williams, R.S. (1998). Differential Expression of Mitochondrial DNA Replication Factors in Mammalian Tissues. Journal of Biological Chemistry *273*, 3447-3451. 10.1074/jbc.273.6.3447.
16. Amiri, M., and Hollenbeck, P.J. (2008). Mitochondrial biogenesis in the axons of vertebrate peripheral neurons. Dev Neurobiol *68*, 1348-1361. 10.1002/dneu.20668.
17. Cioni, J.M., Lin, J.Q., Holtermann, A.V., Koppers, M., Jakobs, M.A.H., Azizi, A., Turner-Bridger, B., Shigeoka, T., Franze, K., Harris, W.A., and Holt, C.E. (2019). Late Endosomes Act as mRNA Translation Platforms and Sustain Mitochondria in Axons. Cell *176*, 56-72 e15. 10.1016/j.cell.2018.11.030.
18. Kuzniewska, B., Cysewski, D., Wasilewski, M., Sakowska, P., Milek, J., Kulinski, T.M., Winiarski, M., Kozielewicz, P., Knapska, E., Dadlez, M., et al. (2020). Mitochondrial protein biogenesis in the synapse is supported by local translation. EMBO Rep *21*, e48882. 10.15252/embr.201948882.
19. Van Laar, V.S., Arnold, B., Howlett, E.H., Calderon, M.J., St Croix, C.M., Greenamyre, J.T., Sanders, L.H., and Berman, S.B. (2018). Evidence for Compartmentalized Axonal Mitochondrial Biogenesis: Mitochondrial DNA Replication Increases in Distal Axons As an Early Response to Parkinson's Disease-Relevant Stress. J Neurosci *38*, 7505-7515. 10.1523/JNEUROSCI.0541-18.2018.
20. Cardanho-Ramos, C., Simoes, R.A., Wang, Y.Z., Faria-Pereira, A., Bomba-Warczak, E., Craessaerts, K., Spinazzi, M., Savas, J.N., and Morais, V.A. (2024). Local mitochondrial replication in the periphery of neurons requires the eEF1A1 protein and the translation of nuclear-encoded proteins. iScience *27*, 109136. 10.1016/j.isci.2024.109136.
21. Hollenbeck, P.J., and Saxton, W.M. (2005). The axonal transport of mitochondria. J Cell Sci *118*, 5411-5419. 10.1242/jcs.02745.
22. Pilling, A.D., Horiuchi, D., Lively, C.M., and Saxton, W.M. (2006). Kinesin-1 and Dynein are the primary motors for fast transport of mitochondria in Drosophila motor axons. Mol Biol Cell *17*, 2057-2068. 10.1091/mbc.e05-06-0526.
23. Saxton, W.M., and Hollenbeck, P.J. (2012). The axonal transport of mitochondria. J Cell Sci *125*, 2095-2104. 10.1242/jcs.053850.
24. Schnapp, B.J., and Reese, T.S. (1989). Dynein is the motor for retrograde axonal transport of organelles. Proc Natl Acad Sci U S A *86*, 1548-1552. 10.1073/pnas.86.5.1548.
25. Canty, J.T., Hensley, A., Aslan, M., Jack, A., and Yildiz, A. (2023). TRAK adaptors regulate the recruitment and activation of dynein and kinesin in mitochondrial transport. Nat Commun *14*, 1376. 10.1038/s41467-023-36945-8.
26. Glater, E.E., Megeath, L.J., Stowers, R.S., and Schwarz, T.L. (2006). Axonal transport of mitochondria requires milton to recruit kinesin heavy chain and is light chain independent. J Cell Biol *173*, 545-557. 10.1083/jcb.200601067.

923 27. Stowers, R.S., Megeath, L.J., Gorska-Andrzejak, J., Meinertzhagen, I.A., and Schwarz,
924 T.L. (2002). Axonal transport of mitochondria to synapses depends on milton, a novel
925 Drosophila protein. Neuron *36*, 1063-1077. 10.1016/s0896-6273(02)01094-2.
926 28. Guo, X., Macleod, G.T., Wellington, A., Hu, F., Panchumarthi, S., Schoenfield, M.,
927 Marin, L., Charlton, M.P., Atwood, H.L., and Zinsmaier, K.E. (2005). The GTPase dMiro
928 is required for axonal transport of mitochondria to Drosophila synapses. Neuron *47*, 379-
929 393. 10.1016/j.neuron.2005.06.027.
930 29. Fenton, A.R., Jongens, T.A., and Holzbaur, E.L.F. (2021). Mitochondrial adaptor TRAK2
931 activates and functionally links opposing kinesin and dynein motors. Nat Commun *12*,
932 4578. 10.1038/s41467-021-24862-7.
933 30. MacAskill, A.F., Brickley, K., Stephenson, F.A., and Kittler, J.T. (2009). GTPase
934 dependent recruitment of Grif-1 by Miro1 regulates mitochondrial trafficking in
935 hippocampal neurons. Mol Cell Neurosci *40*, 301-312. 10.1016/j.mcn.2008.10.016.
936 31. MacAskill, A.F., and Kittler, J.T. (2010). Control of mitochondrial transport and
937 localization in neurons. Trends Cell Biol *20*, 102-112. 10.1016/j.tcb.2009.11.002.
938 32. Han, S.M., Baig, H.S., and Hammarlund, M. (2016). Mitochondria Localize to Injured
939 Axons to Support Regeneration. Neuron *92*, 1308-1323. 10.1016/j.neuron.2016.11.025.
940 33. Zhou, B., Yu, P., Lin, M.Y., Sun, T., Chen, Y., and Sheng, Z.H. (2016). Facilitation of
941 axon regeneration by enhancing mitochondrial transport and rescuing energy deficits. J
942 Cell Biol *214*, 103-119. 10.1083/jcb.201605101.
943 34. Campbell, P.D., Shen, K., Sapio, M.R., Glenn, T.D., Talbot, W.S., and Marlow, F.L.
944 (2014). Unique function of Kinesin Kif5A in localization of mitochondria in axons. J
945 Neurosci *34*, 14717-14732. 10.1523/JNEUROSCI.2770-14.2014.
946 35. Drerup, C.M., Herbert, A.L., Monk, K.R., and Nechiporuk, A.V. (2017). Regulation of
947 mitochondria-dynactin interaction and mitochondrial retr ograde transport in axons. eLife
948 *6*, e22234. 10.7554/eLife.22234.
949 36. Joshi, D.C., Zhang, C.L., Babujee, L., Vevea, J.D., August, B.K., Sheng, Z.H., Chapman,
950 E.R., Gomez, T.M., and Chiu, S.Y. (2019). Inappropriate Intrusion of an Axonal
951 Mitochondrial Anchor into Dendrites Causes Neurodegeneration. Cell Rep *29*, 685-696
952 e685. 10.1016/j.celrep.2019.09.012.
953 37. Mandal, A., Wong, H.-T.C., Pinter, K., Mosqueda, N., Beirl, A., Lomash, R.M., Won, S.,
954 Kindt, K.S., and Drerup, C.M. (2021). Retrograde Mitochondrial Transport Is Essential
955 for Organelle Distribution and Health in Zebrafish Neurons. The Journal of Neuroscience
956 *41*, 1371-1392. 10.1523/JNEUROSCI.1316-20.2020.
957 38. Metcalfe, W.K., Kimmel, C.B., and Schabtach, E. (1985). Anatomy of the posterior
958 lateral line system in young larvae of the zebrafish. The Journal of Comparative
959 Neurology *233*, 377-389. 10.1002/cne.902330307.
960 39. Kindt, Katie S., Finch, G., and Nicolson, T. (2012). Kinocilia Mediate
961 Mechanosensitivity in Developing Zebrafish Hair Cells. Developmental Cell *23*, 329-
962 341. 10.1016/j.devcel.2012.05.022.
963 40. Eckley, D.M., and Schroer, T.A. (2003). Interactions between the evolutionarily
964 conserved, actin-related protein, Arp11, actin, and Arp1. Mol Biol Cell *14*, 2645-2654.
965 10.1091/mbc.e03-01-0049.
966 41. Choi, H.M.T., Schwarzkopf, M., Fornace, M.E., Acharya, A., Artavanis, G., Stegmaier, J.,
967 Cunha, A., and Pierce, N.A. (2018). Third-generation in situ hybridization chain reaction:

968 multiplexed, quantitative, sensitive, versatile, robust. Development *145*, dev165753.
969 10.1242/dev.165753.
970 42. Kawano, D., Pinter, K., Chlebowski, M., Petralia, R.S., Wang, Y.-X., Nechiporuk, A.V.,
971 and Drerup, C.M. (2022). NudC regulated Lis1 stability is essential for the maintenance
972 of dynamic microtubule ends in axon terminals. iScience *25*, 105072.
973 10.1016/j.isci.2022.105072.
974 43. Lloyd, Thomas E., Machamer, J., O'Hara, K., Kim, Ji H., Collins, Sarah E., Wong,
975 Man Y., Sahin, B., Imlach, W., Yang, Y., Levitan, Edwin S., et al. (2012). The p150Glued
976 CAP-Gly Domain Regulates Initiation of Retrograde Transp ort at Synaptic Termini.
977 Neuron *74*, 344-360. 10.1016/j.neuron.2012.02.026.
978 44. McGrail, M., Gepner, J., Silvanovich, A., Ludmann, S., Serr, M., and Hays, T.S. (1995).
979 Regulation of cytoplasmic dynein function in vivo by the Drosophila Glued complex.
980 The Journal of cell biology *131*, 411-425. 10.1083/jcb.131.2.411.
981 45. Moughamian, Armen J., and Holzbaur, Erika L.F. (2012). Dynactin Is Required for
982 Transport Initiation from the Distal Axon. Neuron *74*, 331-343.
983 10.1016/j.neuron.2012.02.025.
984 46. Young, M.J., Humble, M.M., DeBalsi, K.L., Sun, K.Y., and Copeland, W.C. (2015).
985 POLG2 disease variants: analyses reveal a dominant negative heterodimer, altered
986 mitochondrial localization and impaired respiratory capacity. Hum Mol Genet *24*, 5184-
987 5197. 10.1093/hmg/ddv240.
988 47. Rajala, N., Gerhold, J.M., Martinsson, P., Klymov, A., and Spelbrink, J.N. (2014).
989 Replication factors transiently associate with mtDNA at the mitochondrial inner
990 membrane to facilitate replication. Nucleic Acids Research *42*, 952-967.
991 10.1093/nar/gkt988.
992 48. Kaufman, B.A., Durisic, N., Mativetsky, J.M., Costantino, S., Hancock, M.A., Grutter, P.,
993 and Shoubridge, E.A. (2007). The Mitochondrial Transcription Factor TFAM Coordinates
994 the Assembly of Multiple DNA Molecules into Nucleoid-like Structures. Molecular
995 Biology of the Cell *18*, 3225-3236. 10.1091/mbc.e07-05-0404.
996 49. Rath, S., Sharma, R., Gupta, R., Ast, T., Chan, C., Durham, T.J., Goodman, R.P.,
997 Grabarek, Z., Haas, M.E., Hung, W.H.W., et al. (2020). MitoCarta3.0: an updated
998 mitochondrial proteome now with sub-organelle localization and pathway annotations.
999 Nucleic Acids Research *49*, D1541-D1547. 10.1093/nar/gkaa1011.
1000 50. Ghysen, A., and Dambly-Chaudiere, C. (2005). The three-sided romance of the lateral
1001 line: glia love axons love precursors love glia. Bioessays *27*, 488-494.
1002 10.1002/bies.20225.
1003 51. Wong, H.-T.C., Lang, A.E., Stein, C., and Drerup, C.M. (2024). ALS-Linked VapB P56S
1004 Mutation Alters Neuronal Mitochondrial Turnover at the Synapse. The Journal of
1005 Neuroscience *44*, e0879242024. 10.1523/JNEUROSCI.0879-24.2024.
1006 52. Mandal, A., Pinter, K., and Drerup, C.M. (2018). Analyzing Neuronal Mitochondria in
1007 vivo Using Fluorescent Reporters in Zebrafish. Frontiers in Cell and Developmental
1008 Biology *6*, 144. 10.3389/fcell.2018.00144.
1009 53. Kageyama, Y., Zhang, Z., Roda, R., Fukaya, M., Wakabayashi, J., Wakabayashi, N.,
1010 Kensler, T.W., Reddy, P.H., Iijima, M., and Sesaki, H. (2012). Mitochondrial division
1011 ensures the survival of postmitotic neurons by suppressing oxidative damage. J Cell Biol
1012 *197*, 535-551. 10.1083/jcb.201110034.

1013 54. Smirnova, E., Griparic, L., Shurland, D.L., and van der Bliek, A.M. (2001). Dynamin-
1014 related protein Drp1 is required for mitochondrial division in mammalian cells. Mol Biol
1015 Cell *12*, 2245-2256. 10.1091/mbc.12.8.2245.
1016 55. Zhu, P.P., Patterson, A., Stadler, J., Seeburg, D.P., Sheng, M., and Blackstone, C. (2004).
1017 Intra- and intermolecular domain interactions of the C-terminal GTPase effector domain
1018 of the multimeric dynamin-like GTPase Drp1. J Biol Chem *279*, 35967-35974.
1019 10.1074/jbc.M404105200.
1020 56. Renken, C.J., Kim, S., Wu, Y., Hammarlund, M., and Yogev, S. (2024). Cytoplasmic
1021 ribosomes hitchhike on mitochondria to dendrites. 10.1101/2024.09.13.612863.
1022 57. Horie, C., Suzuki, H., Sakaguchi, M., and Mihara, K. (2002). Characterization of Signal
1023 That Directs C-Tail–anchored Proteins to Mammalian Mitochondrial Outer Membrane.
1024 Molecular Biology of the Cell *13*, 1615-1625. 10.1091/mbc.01-12-0570.
1025 58. Yang, R., Bentley, M., Huang, C.-F., and Banker, G. (2016). Analyzing kinesin motor
1026 domain translocation in cultured hippocampal neurons. In Methods in Cell Biology,
1027 (Elsevier), pp. 217-232.
1028 59. Eichner, L.J., and Giguère, V. (2011). Estrogen related receptors (ERRs): A new dawn in
1029 transcriptional control of mitochondrial gene networks. Mitochondrion *11*, 544-552.
1030 10.1016/j.mito.2011.03.121.
1031 60. Hock, M.B., and Kralli, A. (2009). Transcriptional Control of Mitochondrial Biogenesis
1032 and Function. Annual Review of Physiology *71*, 177-203.
1033 10.1146/annurev.physiol.010908.163119.
1034 61. Fan, W., He, N., Lin, C.S., Wei, Z., Hah, N., Waizenegger, W., He, M.-X., Liddle, C., Yu,
1035 R.T., Atkins, A.R., et al. (2018). ERRγ Promotes Angiogenesis, Mitochondrial
1036 Biogenesis, and Oxidative Remodeling in PGC1α/β-Deficient Muscle. Cell Reports *22*,
1037 2521-2529. 10.1016/j.celrep.2018.02.047.
1038 62. Huss, J.M., Torra, I.P., Staels, B., Giguère, V., and Kelly, D.P. (2004). Estrogen-Related
1039 Receptor α Directs Peroxisome Proliferator-Activated Receptor α Signaling in the
1040 Transcriptional Control of Energy Metabolism in Cardiac and Skeletal Muscle. Molecular
1041 and Cellular Biology *24*, 9079-9091. 10.1128/MCB.24.20.9079-9091.2004.
1042 63. Pei, L., Mu, Y., Leblanc, M., Alaynick, W., Barish, Grant D., Pankratz, M., Tseng,
1043 Tiffany W., Kaufman, S., Liddle, C., Yu, Ruth T., et al. (2015). Dependence of
1044 Hippocampal Function on ERRγ-Regulated Mitochondrial Metabolism. Cell Metabolism
1045 *21*, 628-636. 10.1016/j.cmet.2015.03.004.
1046 64. Howitz, K.T., Bitterman, K.J., Cohen, H.Y., Lamming, D.W., Lavu, S., Wood, J.G.,
1047 Zipkin, R.E., Chung, P., Kisielewski, A., Zhang, L.-L., et al. (2003). Small molecule
1048 activators of sirtuins extend Saccharomyces cerevisiae lifespan. Nature *425*, 191-196.
1049 10.1038/nature01960.
1050 65. Lopes Costa, A., Le Bachelier, C., Mathieu, L., Rotig, A., Boneh, A., De Lonlay, P.,
1051 Tarnopolsky, M.A., Thorburn, D.R., Bastin, J., and Djouadi, F. (2014). Beneficial effects
1052 of resveratrol on respiratory chain defects in patients' fibroblasts involve estrogen
1053 receptor and estrogen-related receptor alpha signaling. Human Molecular Genetics *23*,
1054 2106-2119. 10.1093/hmg/ddt603.
1055 66. Sopariwala, D.H., Rios, A.S., Park, M.K., Song, M.S., Kumar, A., and Narkar, V.A.
1056 (2022). Estrogen-related receptor alpha is an AMPK -regulated factor that promotes
1057 ischemic muscle revascularization and recovery in diet-induced obese mice. FASEB
1058 BioAdvances *4*, 602-618. 10.1096/fba.2022-00015.

1059 67. Wilson, B.J., Tremblay, A.M., Deblois, G., Sylvain-Drolet, G., and Giguère, V. (2010).
1060 An Acetylation Switch Modulates the Transcriptional Activity of Estrogen-Related
1061 Receptor α. Molecular Endocrinology *24*, 1349-1358. 10.1210/me.2009-0441.
1062 68. Yan, M., Audet-Walsh, É., Manteghi, S., Dufour, C.R., Walker, B., Baba, M., St-Pierre, J.,
1063 Giguère, V., and Pause, A. (2016). Chronic AMPK activation via loss of FLCN induces
1064 functional beige adipose tissue through PGC-1α/ERRα. Genes & Development *30*, 1034-
1065 1046. 10.1101/gad.281410.116.
1066 69. Corton, J.M., Gillespie, J.G., Hawley, S.A., and Hardie, D.G. (1995). 5-Aminoimidazole-
1067 4-Carboxamide Ribonucleoside. A Specific Method for Activating AMP-Activated
1068 Protein Kinase in Intact Cells? European Journal of Biochemistry *229*, 558-565.
1069 10.1111/j.1432-1033.1995.tb20498.x.
1070 70. Mosser, E.A., Chiu, C.N., Tamai, T.K., Hirota, T., Li, S., Hui, M., Wang, A., Singh, C.,
1071 Giovanni, A., Kay, S.A., and Prober, D.A. (2019). Identification of pathways that regulate
1072 circadian rhythms using a larval zebrafish small molecule screen. Scientific Reports *9*,
1073 12405. 10.1038/s41598-019-48914-7.
1074 71. Johnston, S.D., Liu, X., Zuo, F., Eisenbraun, T.L., Wiley, S.R., Kraus, R.J., and Mertz,
1075 J.E. (1997). Estrogen-Related Receptor α1 Functionally Binds as a Monomer to Extended
1076 Half-Site Sequences Including Ones Contained within Estrogen-Response Elements.
1077 Molecular Endocrinology *11*, 342-352. 10.1210/mend.11.3.9897.
1078 72. Blander, G., and Guarente, L. (2004). The Sir2 family of protein deacetylases. Annu Rev
1079 Biochem *73*, 417-435. 10.1146/annurev.biochem.73.011303.073651.
1080 73. McMeekin, L.J., Joyce, K.L., Jenkins, L.M., Bohannon, B.M., Patel, K.D., Bohannon,
1081 A.S., Patel, A., Fox, S.N., Simmons, M.S., Day, J.J., et al. (2021). Estrogen-related
1082 Receptor Alpha (ERRα) is Required for PGC-1α-dependent Gene Expression in the
1083 Mouse Brain. Neuroscience *479*, 70-90. 10.1016/j.neuroscience.2021.10.007.
1084 74. Alano, C.C., Tran, A., Tao, R., Ying, W., Karliner, J.S., and Swanson, R.A. (2007).
1085 Differences among cell types in NAD(+) compartmentalization: a comparison of neurons,
1086 astrocytes, and cardiac myocytes. J Neurosci Res *85*, 3378-3385. 10.1002/jnr.21479.
1087 75. Hu, Q., Wu, D., Walker, M., Wang, P., Tian, R., and Wang, W. (2021). Genetically
1088 encoded biosensors for evaluating NAD(+)/NADH ratio in cytosolic and mitochondrial
1089 compartments. Cell Rep Methods *1*. 10.1016/j.crmeth.2021.100116.
1090 76. Wareski, P., Vaarmann, A., Choubey, V., Safiulina, D., Liiv, J., Kuum, M., and Kaasik, A.
1091 (2009). PGC-1α and PGC-1B Regulate Mitochondrial Density in Neurons. Journal of
1092 Biological Chemistry *284*, 21379-21385. 10.1074/jbc.M109.018911.
1093 77. Chen, Y., Jiang, Y., Yang, Y., Huang, X., and Sun, C. (2021). SIRT1 Protects
1094 Dopaminergic Neurons in Parkinson's Disease Models via PGC-1α-Mediated
1095 Mitochondrial Biogenesis. Neurotoxicity Research *39*, 1393-1404. 10.1007/s12640-021-
1096 00392-4.
1097 78. Hatsuda, A., Kurisu, J., Fujishima, K., Kawaguchi, A., Ohno, N., and Kengaku, M.
1098 (2023). Calcium signals tune AMPK activity and mitochondrial homeostasis in dendrites
1099 of developing neurons. Development *150*, dev201930. 10.1242/dev.201930.
1100 79. Eudy, J.D., Yao, S., Weston, M.D., Ma-Edmonds, M., Talmadge, C.B., Cheng, J.J.,
1101 Kimberling, W.J., and Sumegi, J. (1998). Isolation of a Gene Encoding a Novel Member
1102 of the Nuclear Receptor Superfamily from the Critical Region of Usher Syndrome Type
1103 IIa at 1q41. Genomics *50*, 382-384. 10.1006/geno.1998.5345.

1104 80. Giguère, V., Yang, N., Segui, P., and Evans, R.M. (1988). Identification of a new class of
1105 steroid hormone receptors. Nature *331*, 91-94. 10.1038/331091a0.
1106 81. Huss, J.M., Garbacz, W.G., and Xie, W. (2015). Constitutive activities of estrogen-related
1107 receptors: Transcriptional regulation of metabolism by the ERR pathways in health and
1108 disease. Biochimica et Biophysica Acta (BBA) - Molecular Basis of Disease *1852*, 1912-
1109 1927. 10.1016/j.bbadis.2015.06.016.
1110 82. Lydon, J.P., Power, R.F., and Conneely, O.M. (1992). Differential modes of activation
1111 define orphan subclasses within the steroid/thyroid receptor superfamily. Gene Expr *2*,
1112 273-283.
1113 83. Vernier, M., and Giguère, V. (2021). Aging, senescence and mitochondria: the PGC-
1114 1/ERR axis. Journal of Molecular Endocrinology *66*, R1-R14. 10.1530/JME-20-0196.
1115 84. Yu, L., and Yang, S.J. (2010). AMP-activated protein kinase mediates activity-dependent
1116 regulation of peroxisome proliferator-activated receptor γ coactivator-1α and nuclear
1117 respiratory factor 1 expression in rat visual cortical neurons. Neuroscience *169*, 23-38.
1118 10.1016/j.neuroscience.2010.04.063.
1119 85. Lagouge, M., Argmann, C., Gerhart-Hines, Z., Meziane, H., Lerin, C., Daussin, F.,
1120 Messadeq, N., Milne, J., Lambert, P., Elliott, P., et al. (2006). Resveratrol Improves
1121 Mitochondrial Function and Protects against Metabolic Disease by Activating SIRT1 and
1122 PGC-1α. Cell *127*, 1109-1122. 10.1016/j.cell.2006.11.013.
1123 86. Michishita, E., Park, J.Y., Burneskis, J.M., Barrett, J.C., and Horikawa, I. (2005).
1124 Evolutionarily conserved and nonconserved cellular localizations and functions of human
1125 SIRT proteins. Mol Biol Cell *16*, 4623-4635. 10.1091/mbc.e05-01-0033.
1126 87. Qin, W., Haroutunian, V., Katsel, P., Cardozo, C.P., Ho, L., Buxbaum, J.D., and Pasinetti,
1127 G.M. (2009). PGC-1α Expression Decreases in the Alzheimer Disease Brain as a
1128 Function of Dementia. Archives of Neurology *66*. 10.1001/archneurol.2008.588.
1129 88. Sheng, B., Wang, X., Su, B., Lee, H.-g., Casadesus, G., Perry, G., and Zhu, X. (2012).
1130 Impaired mitochondrial biogenesis contributes to mitochondrial dysfunction in
1131 Alzheimer's disease: Impaired mitochondrial biogenesis in AD. Journal of
1132 Neurochemistry *120*, 419-429. 10.1111/j.1471-4159.2011.07581.x.
1133 89. Shin, J.-H., Ko, Han S., Kang, H., Lee, Y., Lee, Y.-I., Pletinkova, O., Troconso, Juan C.,
1134 Dawson, Valina L., and Dawson, Ted M. (2011). PARIS (ZNF746) Repression of PGC-
1135 1α Contributes to Neurodegeneration in Parkinson's Disease. Cell *144*, 689-702.
1136 10.1016/j.cell.2011.02.010.
1137 90. Stevens, D.A., Lee, Y., Kang, H.C., Lee, B.D., Lee, Y.-I., Bower, A., Jiang, H., Kang, S.-
1138 U., Andrabi, S.A., Dawson, V.L., et al. (2015). Parkin loss leads to PARIS-dependent
1139 declines in mitochondrial mass and respiration. Proceedings of the National Academy of
1140 Sciences *112*, 11696-11701. 10.1073/pnas.1500624112.
1141 91. Westerfield, M. (1993). The zebrafish book: a guide for the laboratory use of zebrafish
1142 (Brachydanio rerio).
1143 92. Kimmel, C.B., Ballard, W.W., Kimmel, S.R., Ullmann, B., and Schilling, T.F. (1995).
1144 Stages of embryonic development of the zebrafish. Developmental Dynamics *203*, 253-
1145 310. 10.1002/aja.1002030302.
1146 93. Kwan, K.M., Fujimoto, E., Grabher, C., Mangum, B.D., Hardy, M.E., Campbell, D.S.,
1147 Parant, J.M., Yost, H.J., Kanki, J.P., and Chien, C.B. (2007). The Tol2kit: A multisite
1148 gateway-based construction kit for Tol2 transposon transgenesis constructs.
1149 Developmental Dynamics *236*, 3088-3099. 10.1002/dvdy.21343.

1150 94. Gibson, D.G., Young, L., Chuang, R.-Y., Venter, J.C., Hutchison, C.A., and Smith, H.O.
1151 (2009). Enzymatic assembly of DNA molecules up to several hundred kilobases. Nature
1152 Methods *6*, 343-345. 10.1038/nmeth.1318.
1153 95. Huang, C.f., and Banker, G. (2012). The Translocation Selectivity of the Kinesins that
1154 Mediate Neuronal Organelle Transport. Traffic *13*, 549-564. 10.1111/j.1600-
1155 0854.2011.01325.x.
1156 96. Cambronne, X.A., Stewart, M.L., Kim, D., Jones-Brunette, A.M., Morgan, R.K., Farrens,
1157 D.L., Cohen, M.S., and Goodman, R.H. (2016). Biosensor reveals multiple sources for
1158 mitochondrial NAD(+). Science *352*, 1474-1477. 10.1126/science.aad5168.
1159 97. Zhang, Q., Li, S., Wong, H.C., He, X.J., Beirl, A., Petralia, R.S., Wang, Y.X., and Kindt,
1160 K.S. (2018). Synaptically silent sensory hair cells in zebrafish are recruited after damage.
1161 Nat Commun *9*, 1388. 10.1038/s41467-018-03806-8.
1162 98. Mo, W., and Nicolson, T. (2011). Both Pre- and Postsynaptic Activity of Nsf Prevents
1163 Degeneration of Hair-Cell Synapses. PLoS ONE *6*, e27146.
1164 10.1371/journal.pone.0027146.
1165 99. Drerup, C.M., and Nechiporuk, A.V. (2013). JNK-Interacting Protein 3 Mediates the
1166 Retrograde Transport of Activated c-Jun N-Terminal Kinase and Lysosomes. PLoS
1167 Genetics *9*, e1003303. 10.1371/journal.pgen.1003303.
1168 100. Drerup, C.M., and Nechiporuk, A.V. (2016). In vivo analysis of axonal transport in
1169 zebrafish. Methods in cell biology *131*, 311-329. 10.1016/bs.mcb.2015.06.007.
1170 101. Preibisch, S., Saalfeld, S., and Tomancak, P. (2009). Globally optimal stitching of tiled
1171 3D microscopic image acquisitions. Bioinformatics *25*, 1463-1465.
1172 10.1093/bioinformatics/btp184.
1173 102. Schindelin, J., Arganda-Carreras, I., Frise, E., Kaynig, V., Longair, M., Pietzsch, T.,
1174 Preibisch, S., Rueden, C., Saalfeld, S., Schmid, B., et al. (2012). Fiji: an open-source
1175 platform for biological-image analysis. Nature Methods *9*, 676-682. 10.1038/nmeth.2019.
1176 103. Thisse, C., and Thisse, B. (2008). High-resolution in situ hybridization to whole-mount
1177 zebrafish embryos. Nature Protocols *3*, 59-69. 10.1038/nprot.2007.514.
1178 104. Logel, J., Dill, D., and Leonard, S. (1992). Synthesis of cRNA probes from PCR-
1179 generated DNA. BioTechniques *13*, 604-610.
1180 105. Bolger, A.M., Lohse, M., and Usadel, B. (2014). Trimmomatic: a flexible trimmer for
1181 Illumina sequence data. Bioinformatics *30*, 2114-2120. 10.1093/bioinformatics/btu170.
1182 106. Dobin, A., Davis, C.A., Schlesinger, F., Drenkow, J., Zaleski, C., Jha, S., Batut, P.,
1183 Chaisson, M., and Gingeras, T.R. (2013). STAR: ultrafast universal RNA-seq aligner.
1184 Bioinformatics *29*, 15-21. 10.1093/bioinformatics/bts635.
1185 107. Liao, Y., Smyth, G.K., and Shi, W. (2014). featureCounts: an efficient general purpose
1186 program for assigning sequence reads to genomic features. Bioinformatics *30*, 923-930.
1187 10.1093/bioinformatics/btt656.
1188 108. Love, M.I., Huber, W., and Anders, S. (2014). Moderated estimation of fold change and
1189 dispersion for RNA-seq data with DESeq2. Genome Biology *15*, 550. 10.1186/s13059-
1190 014-0550-8.
1191 109. Yu, G. (2024). Thirteen years of clusterProfiler. The Innovation *5*, 100722.
1192 10.1016/j.xinn.2024.100722.
1193 110. Kolberg, L., Raudvere, U., Kuzmin, I., Adler, P., Vilo, J., and Peterson, H. (2023).
1194 g:Profiler—interoperable web service for functional enrichment analysis and gene

1195 identifier mapping (2023 update). Nucleic Acids Research *51*, W207-W212.
1196 10.1093/nar/gkad347.
1197 111. Puente-Santamaria, L., Wasserman, W.W., and Del Peso, L. (2019). TFEA.ChIP: a tool
1198 kit for transcription factor binding site enrichment analysis capitalizing on ChIP-seq
1199 datasets. Bioinformatics *35*, 5339-5340. 10.1093/bioinformatics/btz573.
1200 112. Elizarraras, J.M., Liao, Y., Shi, Z., Zhu, Q., Pico, Alexander R., and Zhang, B. (2024).
1201 WebGestalt 2024: faster gene set analysis and new support for metabolomics and multi-
1202 omics. Nucleic Acids Research *52*, W415-W421. 10.1093/nar/gkae456.
1203 113. Wickham, H. (2016). ggplot2: Elegant Graphics for Data Analysis, 2nd 2016 Edition
1204 (Springer International Publishing : Imprint: Springer).
1205 114. Lister, J.A., Robertson, C.P., Lepage, T., Johnson, S.L., and Raible, D.W. (1999). nacre
1206 encodes a zebrafish microphthalmia-related protein that regulates neural-crest-derived
1207 pigment cell fate. Development *126*, 3757-3767. 10.1242/dev.126.17.3757.
1208 115. Obholzer, N., Wolfson, S., Trapani, J.G., Mo, W., Nechiporuk, A., Busch-Nentwich, E.,
1209 Seiler, C., Sidi, S., Söllner, C., Duncan, R.N., et al. (2008). Vesicular Glutamate
1210 Transporter 3 Is Required for Synaptic Transmission in Zebrafish Hair Cells. The Journal
1211 of Neuroscience *28*, 2110-2118. 10.1523/JNEUROSCI.5230-07.2008.

1212
1213